3D Printable Gelatin Methacryloyl (GelMA)-Dextran Aqueous Two-Phase System with Tunable Pores Structure and Size Enables Physiological Behavior of Embedded Cells In Vitro

Ghazi Ben Messaoud, Sanja Aveic, Mattis Wachendoerfer, Horst Fischer, Walter Richtering

RESEARCH ARTICLE

NANO · MICRO small
www.small-journal.com

3D Printable Gelatin Methacryloyl (GelMA)-Dextran Aqueous Two-Phase System with Tunable Pores Structure and Size Enables Physiological Behavior of Embedded Cells In Vitro

Ghazi Ben Messaoud, Sanja Aveic, Mattis Wachendoerfer, Horst Fischer,* and Walter Richtering**

The restricted porosity of most hydrogels established for in vitro 3D tissue engineering applications limits embedded cells with regard to their physiological spreading, proliferation, and migration behavior. To overcome these confines, porous hydrogels derived from aqueous two-phase systems (ATPS) are an interesting alternative. However, while developing hydrogels with trapped pores is widespread, the design of bicontinuous hydrogels is still challenging. Herein, an ATPS consisting of photo-crosslinkable gelatin methacryloyl (GelMA) and dextran is presented. The phase behavior, monophasic or biphasic, is tuned via the pH and dextran concentration. This, in turn, allows the formation of hydrogels with three distinct microstructures: homogenous nonporous, regular disconnected-pores, and bicontinuous with interconnected-pores. The pore size of the latter two hydrogels can be tuned from ≈4 to 100 µm. Cytocompatibility of the generated ATPS hydrogels is confirmed by testing the viability of stromal and tumor cells. Their distribution and growth pattern are cell-type specific but are also strongly defined by the microstructure of the hydrogel. Finally, it is demonstrated that the unique porous structure is sustained when processing the bicontinuous system by inkjet and microextrusion techniques. The proposed ATPS hydrogels hold great potential for 3D tissue engineering applications due to their unique tunable interconnected porosity.

1. Introduction

Polymeric hydrogels are 3D networks that can absorb and retain a large amount of water while preserving their structure. This makes them ideally suited for their use in tissue engineering as substitutes for the natural extracellular matrix (ECM). Hydrogels are generally synthesized using either natural, semi-synthetic, or synthetic polymers.[1] While natural polymers such as collagen and gelatin offer more suitable biological properties as they exhibit cell-adhesive motifs, synthetic polymers can be tuned with tailored mechanical properties.[2] For this reason, semi-synthetic polymers providing the advantages of both natural and synthetic polymers are attractive candidates for developing biomaterials that can be explored as cell, growth factor, and drug carriers in regenerative medicine and a wide variety of in vitro biological studies.[3]

Apart from its biological and mechanical characteristics, the hydrogel's porosity is essential for proper tissue formation and

G. Ben Messaoud[+], W. Richtering
Institute of Physical Chemistry
RWTH Aachen University
Landoltweg 2, European Union, 52074 Aachen, Germany
E-mail: benmessaoud@dwi.rwth-aachen.de; richtering@rwth-aachen.de

The ORCID identification number(s) for the author(s) of this article can be found under https://doi.org/10.1002/smll.202208089

[+]Present address: STLO, INRAE, Institut Agro, 65 rue de Saint-Brieuc, European Union, Rennes 35042, France

DOI: 10.1002/smll.202208089

G. Ben Messaoud[+], W. Richtering
DWI-Leibniz Institute for Interactive Materials
Forckenbeckstrasse 50, European Union, 52074 Aachen, Germany

S. Aveic, M. Wachendoerfer, H. Fischer
Department of Dental Materials and Biomaterials Research
RWTH Aachen University Hospital
52074 Aachen, Germany
E-mail: hfischer@ukaachen.de

function.[4] Similarly, mass transfer limitations within hydrogels above the micrometer scale pose a critical barrier for a more widespread use of engineered hydrogels in diverse in vitro and in vivo applications.[5,6] Adequate hydrogel porosity is therefore essential for homogeneous cell distribution and interconnection throughout the engineered scaffolds. Fine-tuning of the pore size is crucial for favoring physiological tissue regeneration.[7] The minimum pore size is determined by several parameters, including cell type and function. For example, a pore size larger than 30 μm is required for nutrient diffusion within scaffolds via blood vessels.[8] On the other hand, pore sizes ranging from 120 to 325 μm and 200 to 250 μm are ideal for the proliferation and migration of osteoblast and human dermal fibroblast cells, respectively.[9,10]

In addition to the size of the pores, interconnectivity is a determining factor for a functional scaffold to allow infiltration of cells into all its parts and a corollary distribution of oxygen and nutrients or even metabolic waste removal.[11–13] If interconnected porosity is not provided, the efficacy of nutrients and oxygen delivery to the cells is compromised, particularly when the length scale exceeds 100 μm.[14,15] In this regard, several strategies have been applied to control a hydrogel's porosity by regulating the pore size.[16] Hydrogels with porosity from a few to several hundred micrometers can be generated using different techniques. Their macroscale control is based on solvent casting, particle leaching, gas foaming, or freeze-drying techniques.[16] In contrast, fine porosity control at the microscale is based on approaches like the fabrication of microchannels or interconnected microvascular-like networks.[16] Otherwise, microporous hydrogels can be prepared via manufacturing techniques like electrospinning and 3D printing.[5] 3D printing has attained great importance as it enables the 3D preorganization within a hydrogel matrix of different cell types to resemble the microanatomical arrangements. Such a spatial cellular preorganization promotes the physiological maturation of the cell-laden objects towards functional tissues during the subsequent postprinting cultivation process.[17] Microextrusion-based 3D printing techniques can be conducted using viscous pregel systems, however, the resolution and geometrical complexity of the printed cell-laden structures are still limited.[18] Recently, interconnected microporous granular hydrogel composed of microgels of gelatin methacryloyl (GelMA) and silicate nanoparticles was fabricated by microextrusion.[19] The inkjet-based 3D printing technique that uses the drop-on-demand principle requires low-viscosity fluids, resulting in a much higher printing resolution and allowing for the fabrication of complex geometry constructs.[20]

Alternatively, the properties of hydrogels can be tuned via polymer blending. In general, a polymer-polymer mixture in a solvent can be stable (when the two compounds are co-soluble) or unstable (when the two compounds are not cosoluble) depending on the type of interactions between them. These interactions can be associative (formation of soluble or insoluble complexes) or repulsive (demixing).[21] Repulsive interactions lead to the formation of aqueous two-phase systems (ATPS), widely used to separate and purify biomolecules and cells.[22]

During the last decade, preparing functional systems based on ATPS has drawn much attention. For instance, high-order emulsion drops were developed by osmosis-driven phase separation.[23] Porous hydrogels for biomedical,[13,24,25] membrane filtration,[26] energy storage,[27] and art restoration[28] applications have been developed. Their preparation is based on the gelation of one polymer phase, while the second polymer acts as a sacrificial template to induce microscale porosity in the final hydrogel structure. Compared to classical organic-in-water emulsions, hydrogels obtained from ATPS also have the advantage of being prepared in a fully aqueous medium suitable for cells growth.[29] The reported ATPS-based hydrogels exhibited generally regular pores resulting from droplet dispersed phase in a continuous gelled phase, whereas bicontinuous structures are mainly lacking.[30–33] Very recently, macroporous bicontinuous hydrogels have shown great potential for neural and tissue engineering applications.[13,25,34,35] However these studies also demonstrated how developing bicontinuous microstructures with reproducible length scale or pores is still challenging.[13,34,36]

In this work, GelMA hydrogels with finely controlled pore structure and size were synthesized starting from the ATPS followed by photo-crosslinking the GelMA phase. GelMA is one of the most frequent choices for tissue engineering applications due to its excellent biocompatibility and highly tunable mechanical properties.[37–41] Gelatin provides integrin-binding RGD (Arg-Gly-Asp) motifs and metalloprotease digestion sites to the GelMA hydrogels, which ensure cell attachment and spreading within hydrogel matrices.[42]

In the absence of attractive interactions, polysaccharide-protein mixtures are highly subjected to thermodynamic incompatibility because of their substantial water affinity difference or depletion interaction forces in the case of nonadsorbent polysaccharide and globular protein mixtures.[43] To induce segregative phase separation, we selected dextran, a neutral biocompatible exopolysaccharide composed of α(1,6)-linked d-glucopyranosyl linear backbone and a small amount of α(1,3)-linked d-glucose. The dextran phase is used as a sacrificial template and is washed out of the hydrogel after the GelMA has been photo-crosslinked.

By finely tuning the pH and dextran concentration, we controlled the phase separation process, which resulted in hydrogels with different microstructures and pore sizes. Moreover, we examined the applicability of the hydrogels with different pore structures for the long-term growth of human mesenchymal stem cells (hMSCs), human periodontal ligament fibroblasts (hPDLFs), human neuroblastoma cells (hNBs), and human endothelial cells (hECs). Finally, we demonstrated the feasibility of printing GelMA-dextran solutions and gels using inkjet and microextrusion techniques, respectively.

2. Results

2.1. Phase Separation Process and Hydrogel Microstructure

The stability of a binary mixture in water depends on the Gibbs energy (ΔG_{mix}) with $\Delta G_{mix} = \Delta H_{mix} - T\Delta S_{mix}$, where ΔH_{mix} is the enthalpy, T is the temperature and ΔS_{mix} is the entropy of mixing. When $\Delta G_{mix} > 0$, the system tends to separate into two distinct phases. The state of thermodynamic equilibrium is reached when ΔG_{mix} is minimal. Protein-polysaccharide mixtures are known to show segregative phase separation under specific physicochemical conditions.[44] Their phase separation is explained commonly by the second virial coefficient model

or, in some cases, using the depletion interaction model for globular protein in the presence of nonadsorbent polysaccharide mixtures.[43] For neutral polymer mixtures, demixing is generally induced by controlling the concentrations and mixture temperature. In the current study, the system comprises GelMA, a polyampholyte containing cationic and anionic ionizable groups, and dextran, a neutral polysaccharide (**Figure 1**A). Demixing of a polyelectrolyte-neutral polymer system crucially depends on the polyelectrolyte charge state. When the polyelectrolyte is charged, demixing, i.e., each component's restriction to each phase, is entropically unfavorable because it would imply the polyelectrolyte counterions' confinement in the polyelectrolyte phase to respect the principle of electroneutrality between the two phases.[45,46] For charged GelMA, inducing segregative phase separation could result from acting on the entropy of mixing by significantly increasing both components' concentrations. This would result in less flexibility in the hydrogel preparation conditions, and increasing GelMA concentration could lead to stiffer hydrogels, which may affect cell behavior.[47] Therefore, inducing segregative phase separation in the present system could be achieved by either adjusting the mixture's pH near the isoelectric point (IEP) of the GelMA to release counterions in the solution or by adding salt, which will screen the effect of counterions.

The IEP point of the synthesized GelMA was determined by monitoring the evolution of its electrophoretic mobility (EM) as a function of pH (Figure 1B). GelMA is a polyampholyte containing both carboxylic acid and amino groups. Increasing the pH led to the deprotonation of the functional charged groups. The EM is negative due to a higher COO^-/COOH ratio compared to NH_3^+ / NH_2. Decreasing the pH leads to a progressive increase of the EM due to a simultaneous increase in the number of the positively charged protonated amino groups (NH_3^+) and uncharged carboxylic groups (COOH) until reaching the IEP, corresponding to equal positive and negative charges. The experimental GelMA IEP is between 4.1 and 4.4. Decreasing the pH further leads to a net positive EM. The GelMA IEP is significantly lower than the IEP of native gelatin type A ($7 < IEP < 9$).[48] This shift is mainly related to the methacrylation reaction occurring on both amino and hydroxyl groups and affecting the final ratio of ionizable groups, i.e., amino: carboxylic acid groups.

To check which role the counterions play in the segregative phase separation process, the influence of pH was investigated for two systems with a selected GelMA concentration of 52.8 mg mL^{-1} and two different dextran concentrations of 12.3 and 24.6 mg mL^{-1} and salt-free conditions. Depending on the pH, one obtains either dextran droplets dispersed in a continuous GelMA phase or a bicontinuous solution, respectively. Typical turbidity curves at 37 °C of GelMA-dextran as a function of pH are shown in Figure 1C. Both GelMA/dextran systems of 52.8/12.3 mg mL^{-1} and 52.8/24.6 mg mL^{-1} are homogenous at a pH near neutral (6.3–6.5) and show no phase separation. The phase separation process as a function of acidification can be described as a set of five different regions: Region 1: at high pH values, generally pH above 5, the mixture is clear and the turbidity is constant; region 2: an abrupt increase in turbidity from a starting pH ≈ 5.1 characterizes this region and reflects the cloudy aspect of the solution; a maximum, constant plateau characterizes region 3, the turbidity profile and the solution have an opalescent aspect in a pH range of $4 < pH < 4.8$; region 4, between pH 4 and pH 3.5 the turbidity decreases progressively; and finally region 5, the solution is clear and homogenous again, and the turbidity is back to its initial value.

The turbidity profile of GelMA-dextran (Figure 1C) and the EM evolution of GelMA as a function of pH (Figure 1B) illustrates the symmetry of the phase separation process vis-a-vis the IEP of GelMA. Furthermore, demixing is suppressed if GelMA is sufficiently charged ($|EM| > 1$) either negatively or positively, highlighting how counterions' entropy drives the phase separation process. Separately, the influence of adding salt (NaCl) on the phase separation was investigated in water at pH of 6.5 for the system, leading to dextran droplets dispersed in GelMA continuous phase (Figure S1, Supporting Information). The GelMA-dextran system was prepared by increasing NaCl and, following the photo-crosslinking step, the microstructure of the resulting hydrogel was investigated by CLSM. The addition of a small amount of NaCl (2.4 mM) leads to segregative phase separation with the formation of dextran droplets dispersed in GelMA continuous phase solution and, therefore, RDP hydrogel following photo-crosslinking. Increasing the NaCl to 50.4 mM led to RDP hydrogel with larger pores while a NaCl molarity of 154 mM (physiological water, NaCl 0.9%) highlighted a decrease in pore size but a relatively monodisperse and high pore density hydrogel (Figure S1, Supporting Information). A constant GelMA concentration of 52.8 mg mL^{-1} in phosphate buffer saline (PBS) demonstrated how the increase in dextran concentration enhanced phase separation and increased the pores of the resulting hydrogel (Figure S2, Supporting Information).

The investigation of the effect of pH and salt highlighted the role of the entropy of counterions as the main parameter of the phase separation process for the current GelMA-dextran system. However, the potential contribution to the phase separation process of the GelMA conformational change effect and chain collapse by decreasing intrachain and interchain repulsion near the isoelectric point (or by charge screening in the case of salt addition) should not be excluded.[48] To control the pore size of the dextran droplets and the length scale of the pores in the bicontinuous system, the influence of small pH and dextran variations on the microstructure of RDP and ICP hydrogels is investigated. Because the pH variation even by 0.1 unit leads to an abrupt variation of the turbidity as shown in Figure 1C, in the following, for more relevancy the results are presented as a function of the acid (HCl) molarity rather than pH.

Figure 1D–G shows the microstructure of regular-disconnected porous (RDP) and interconnected porous (ICP) hydrogel as a function of dextran and HCl molarity. For RDP hydrogels, increasing the HCl molarity for a constant dextran concentration led to a variation of the pore size distribution, however, this variation is not linearly dependent on the HCl amount. In fact, at low HCl molarity, the droplet size is relatively smaller (Figure 1d1,d5), while for an intermediate concentration, the droplets are larger but with a broader size distribution (Figure 1d2,d5). Further increase of the HCl concentration to 20 mM leads to smaller but monodisperse pores (Figure 1d3,d5). However, increasing the HCl molarity to 24 mM led to phase inversion, mirroring the situation observed previously for increasing the dextran concentration (Figure 1d4). Increasing dextran concentration led to an increase in the resulting pore size (Figure 1e1–e3), as highlighted by the pore size distribution

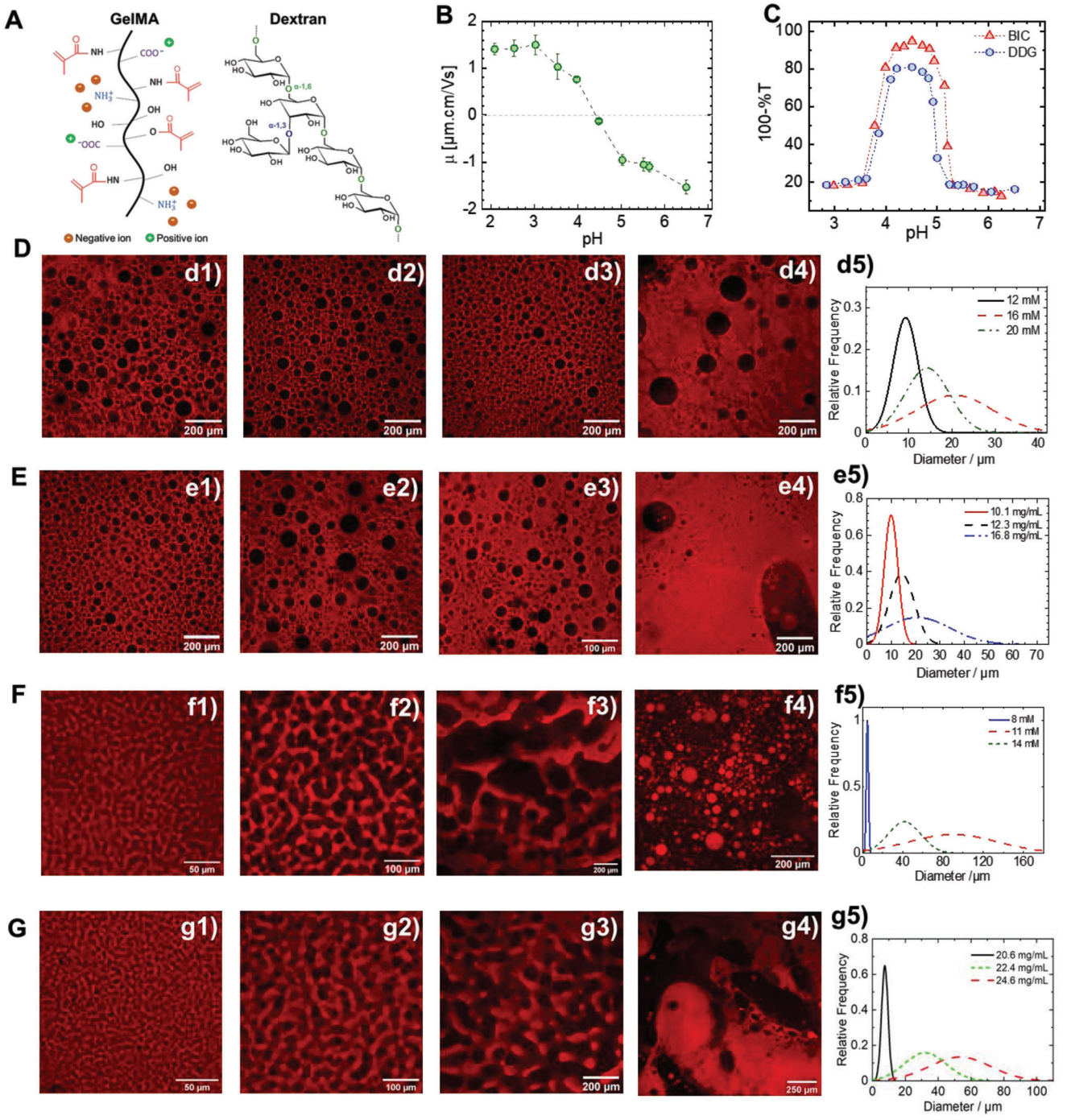

Figure 1. A) Chemical structure of GelMA and dextran, B) pH-dependency of GelMA EM, C) turbidity (100-%T) evolution as a function of pH for bicontinuous (BIC) and dextran droplets dispersed in a continuous GelMA phase (DDG) system. D) Influence of HCl molarity on GelMA (52.8 mg mL^{-1})-dextran (12.3 mg mL^{-1}) mixture on the final hydrogel RDP microstructure. Confocal laser scanning microscopy (CLSM) micrographs of the photo-crosslinked RDP hydrogels obtained with d1) 12, d2) 16, d3) 20, and d4) 24 mM HCl and d5) the respective Gaussian pore size distribution of samples shown in d1-d3. E) Influence of dextran concentration on the final RDP hydrogel microstructure. CLSM micrographs of the photo-crosslinked RDP hydrogels obtained with e1) 10.1, e2) 12.3, e3) 16.8, and e4) 20 mg mL^{-1} of dextran and e5) the respective Gaussian pore size distribution of samples shown in e1-e3. F) Influence of HCl molarity on GelMA (52.8 mg mL^{-1})-dextran (24.6 mg mL^{-1}) mixture on the final hydrogel ICP microstructure. CLSM micrographs of the photo-crosslinked ICP hydrogels obtained with f1) 8, f2) 11, f3) 14, and f4) 20 mM HCl and f5) the respective Gaussian pore size distribution of samples shown in f1-f3. G) Influence of dextran concentration on the final ICP hydrogel microstructure. CLSM micrographs of the photo-crosslinked bicontinuous ICP hydrogels obtained with g1) 20.6, g2) 22.4, g3) 24.6, and g4) 28 mg mL^{-1} of dextran and g5) the respective Gaussian pore size distribution of samples shown in g1-g3. Scale bars indicated for each micrograph.

(Figure 1e5). While further increasing the dextran concentration results in the appearance of some heterogeneities in the hydrogel and some local phase inversion by the formation of GelMA gelled structures dispersed in a continuous dextran phase (Figure 1e4).

A comparable effect of pH and dextran concentration is observed for the bicontinuous system, leading to ICP hydrogels (Figure 1F,G). However, this system is even more sensitive than the RDP system. A slight increase in dextran or HCl concentration led to an abrupt microstructure modification (Figure 1F,G). The significant difference in sensitivity to dextran concentration and the pH of the mixture between the dextran droplets dispersed in GelMA continuous phase and bicontinuous systems is mainly related to their different thermodynamics. Even though the phase separation mechanism is not investigated in the current study, bicontinuous systems are exclusively obtained through spinodal decomposition and for which the system is thermodynamically unstable. Small fluctuations in concentration result in the rapid formation of structures that continuously grow in size. In contrast, dispersed dextran droplets could be obtained through nucleation and growth mechanism and for which the system is thermodynamically metastable. Only concentrations' fluctuations reaching a critical size and amplitude can develop while the others disappear.[49]

Controlling the porosity of the hydrogel is crucial but insufficient for the use of hydrogels in tissue engineering applications. ECM stiffness and stress relaxation behavior are also influential factors in many biological processes and cell functions like induction and differentiation.[50–53] It is well known, for example, that the differentiation dynamic of hMSCs is more pronounced in less stiff hydrogels and that the invasive features of neoplastic cells correlate with the stiffness of the ECM in which they reside.[54] In this regard, the rheological and mechanical properties of NOP, RDP, and ICP hydrogels were examined through compression experiments and small amplitude oscillatory shear (SAOS) rheology. The microstructure of the hydrogels used for compression experiments is shown in **Figure 2**A,B. CLSM highlights the microstructure of these three hydrogel types and SEM images emphasize the characteristic microstructure of each hydrogel type and illustrate the fibrillar feature of the GelMA hydrogels (Figure 2b1). The RDP hydrogels showed individual disconnected pores (Figure 2b2), and imaging the GelMA phase of the IPC hydrogels demonstrates a nanofibrous architecture (Figure 2b3). Preparation for SEM results in overall shrinkage of the fibrous microstructure, however the overall pore structure with pore arrangement and orientation are retained. The pore size analysis of the RDP and ICP hydrogels is shown in (Figure 2C) and reveals a mean RDP and ICP porosity of 12 and 50 μm, respectively.

Typical compression curves of cylindrical hydrogel samples, shown in Figure S3, Supporting Information, highlight two distinct regimes: a linear Hookean regime followed by a densification regime where the stress increased exponentially as a function of the strain. The load failure generally occurs for strains between 0.5 and 0.7 and maximum stresses at rupture vary from 15 to 100 KPa. The stiffness of the GelMA hydrogels was determined from the linear stress-strain relationship for a strain range ≤0.15 (Figure 2D). The average stiffness values are 9.0 ± 1.4 kPa, 13.0 ± 1.5 kPa, and 9.1± 1.5 kPa for NOP, RDP, and ICP hydrogels, respectively. The RDP was significantly stiffer than the NOP and ICP hydrogels.

In this study, the stiffness of the engineered GelMA hydrogels (7.4–14.2 kPa) was significantly higher than reported previously for UV crosslinked GelMA hydrogels of a comparable concentration.[13,55–57] In general, the hydrogel's stiffness for a given GelMA concentration depends on the methacrylation degree and hydrogel's preparation conditions, i. e., photoinitiator concentration, UV intensity, and exposure time.[58] Therefore, the high photoinitiator concentration of 10% (w/w_{GelMA}) and high UV intensity of 30 W at a long exposure time of 4 min could explain why the mechanical properties here were slightly different compared to previous studies.

The measured stiffness values are comparable to those of soft living tissues like kidney, liver, and lung.[59] While the stiffness is not sufficient to characterize the complex mechanical behavior of native tissues,[53] our data suggest that ATPS GelMA hydrogels should integrate well with native tissue without causing failure due to a mechanical mismatch.[60] While the Young modulus provides a static value, SAOS rheology was conducted to characterize the viscoelastic properties of the ATPS hydrogels as a function of frequency and therefore at different time scales is conducted (Figure 2E). For a constant photoinitiator concentration, the gelation kinetics of the GelMA-dextran ATPS solutions depends on the applied UV intensity.

Since the gelation in situ is performed at room temperature (RT), a relatively high UV intensity of 100 mW cm^{-2} during 120 s is selected for fast gelation and quenching of the hydrogel microstructure (Figure S4, Supporting Information). The evolution of *G'* and *G''* as a function of frequency (*f*) demonstrates that *G'* >> *G''* and indicate that the GelMA-dextran ATPS have a predominantly elastic rather than a viscous character with no evidence of frequency dependence of the storage modulus $G' \alpha f^0$. This criterion distinguishes gels from viscous liquids and specifies that the deformation energy is recovered in the elastic stretching of network chains.[61] The ICP hydrogels exhibit a $G' \approx 2.5$ *KPa* lower than the RDP and NOP hydrogels' $G' \approx 4$ *KPa*.

It should be mentioned that the rheological and mechanical properties of ATPS hydrogels depend on the average pore size and density.[24] In general, the mechanical properties of multicomponent hydrogels result from the contribution of each component, depending on their effective volume fractions.[62]

2.2. Cell Behavior in Different GelMA-Dextran ATPS Hydrogels

The observed physicochemical properties of the tunable GelMA-dextran ATPS hydrogels prompted us to investigate their applicability in cell-related studies. All three structures of the ATPS hydrogel, NOP, RDP, and ICP, were applied for the growth of several phenotypically and functionally different cell types (**Figure 3**A), namely hMSCs, hPDLFs, and finally hNBs as an example of cancer cell. The growth of each cell type was probed for 7 days, which was chosen as the experimental endpoint. Each structure effectively sustained the growth of tested cell types while maintaining expected cell morphology: stretched and elongated organization was confirmed for hMSC and hPDLF, whereas rosette-forming cancer cell colonies were favored by hNB cells (Figure 3B–D). The cell organization and distribution

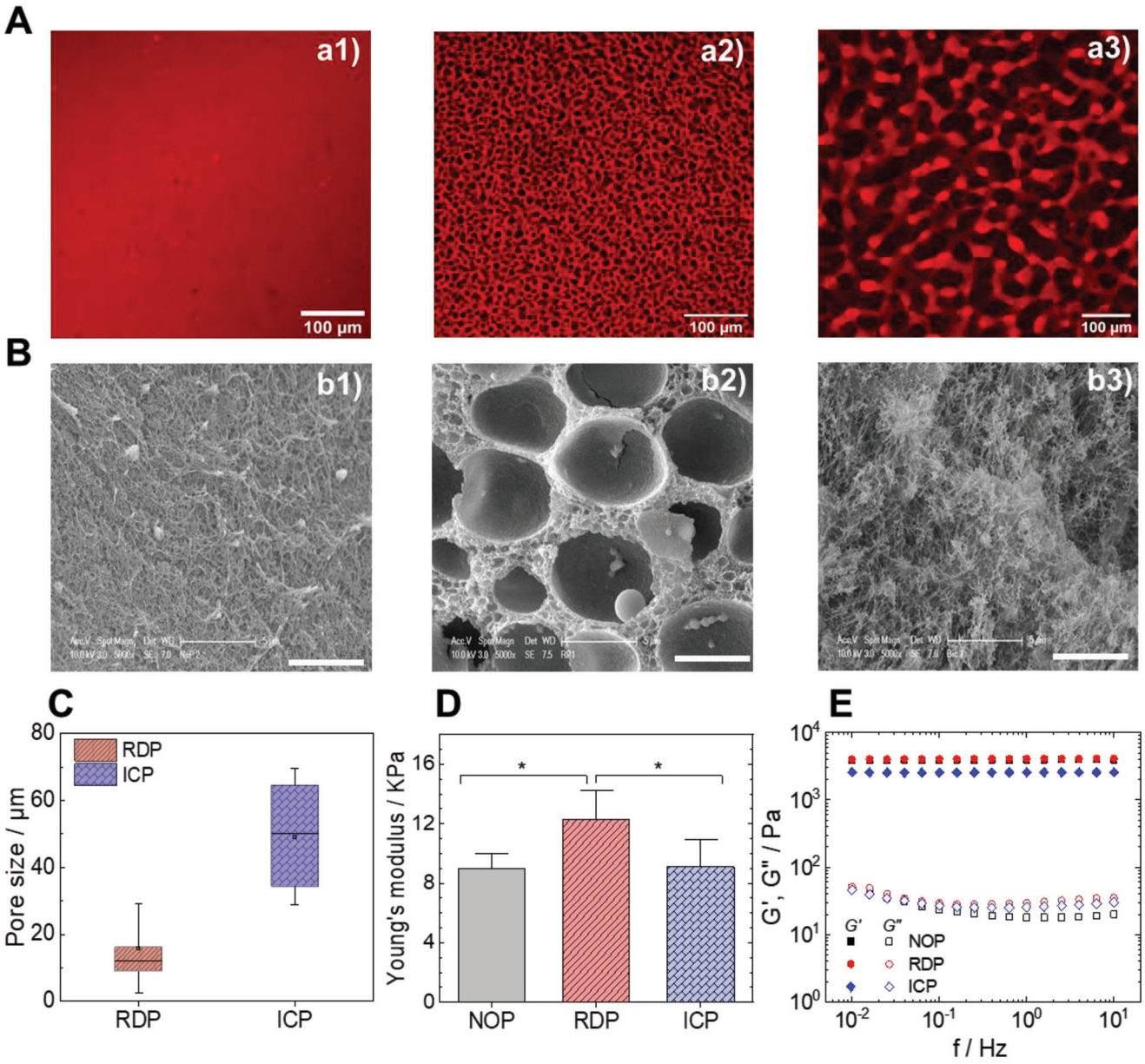

Figure 2. A typical microstructure of the hydrogels used for mechanical experiments investigated using A) CLSM micrographs of a1) NOP, a2) RDP, and a3) ICP hydrogels (scale bar: 100 µm). B) SEM micrographs of the GelMA–dextran ATPS b1) NOP, b2) RDP, and b3) ICP hydrogels (scale bar: 5 µm). C) Average pore size of RDP and ICP hydrogels measured from Figure 2a2,a3, respectively. D) Young's modulus of NOP, RDP, and ICP hydrogels determined from the linear strain stress relationship for a strain up to 0.15 (Figure S5, Supporting Information) and E) frequency-dependent ***G***' (filled) and ***G***'' moduli (open) of NOP, RDP and ICP hydrogels prepared by in situ photo-crosslinking by UV-rheology.

pattern were determined by both variables, ATPS structure, and the cells' (patho)physiological features. As expected, the lack of micrometer-sized voids in the NOP hydrogels allowed the growth of hMSCs and hPDLFs on the surface after seeding, while exhibiting a flat, spread-out appearance comparable to conventional 2D cell growth. In the RDP hydrogels (Figure 3C), the growth of each cell type was highly influenced by pore size favoring their positioning within the pores of medium-high diameter (≈20–50 µm).

Compared with NOP and RDP, the ICP hydrogel allowed a more homogeneous cell distribution and a dense network of cell-to-cell connections for hMSCs and hPDLFs (Figure 3D). Interestingly, hNB cells exhibit their characteristic rosette-like organization[63] with very little or no spreading at all, even in the presence of interconnections inside the hydrogel. None of the hydrogels displayed a negative effect over cell growth in the examinated time frame (Figure 3E) while confirming substantially more accented proliferative capacity of malignant hNB cell respect to normal ones (hMSC and hPDLF). Consistently, each hydrogel type maintained a viability rate of seeded hMSC, hPDLF and hNB cells above 90% after 7 days (Figure 3F). The latter confirms an excellent biocompatibility of the proposed ATPS hydrogels (Figure 3G).

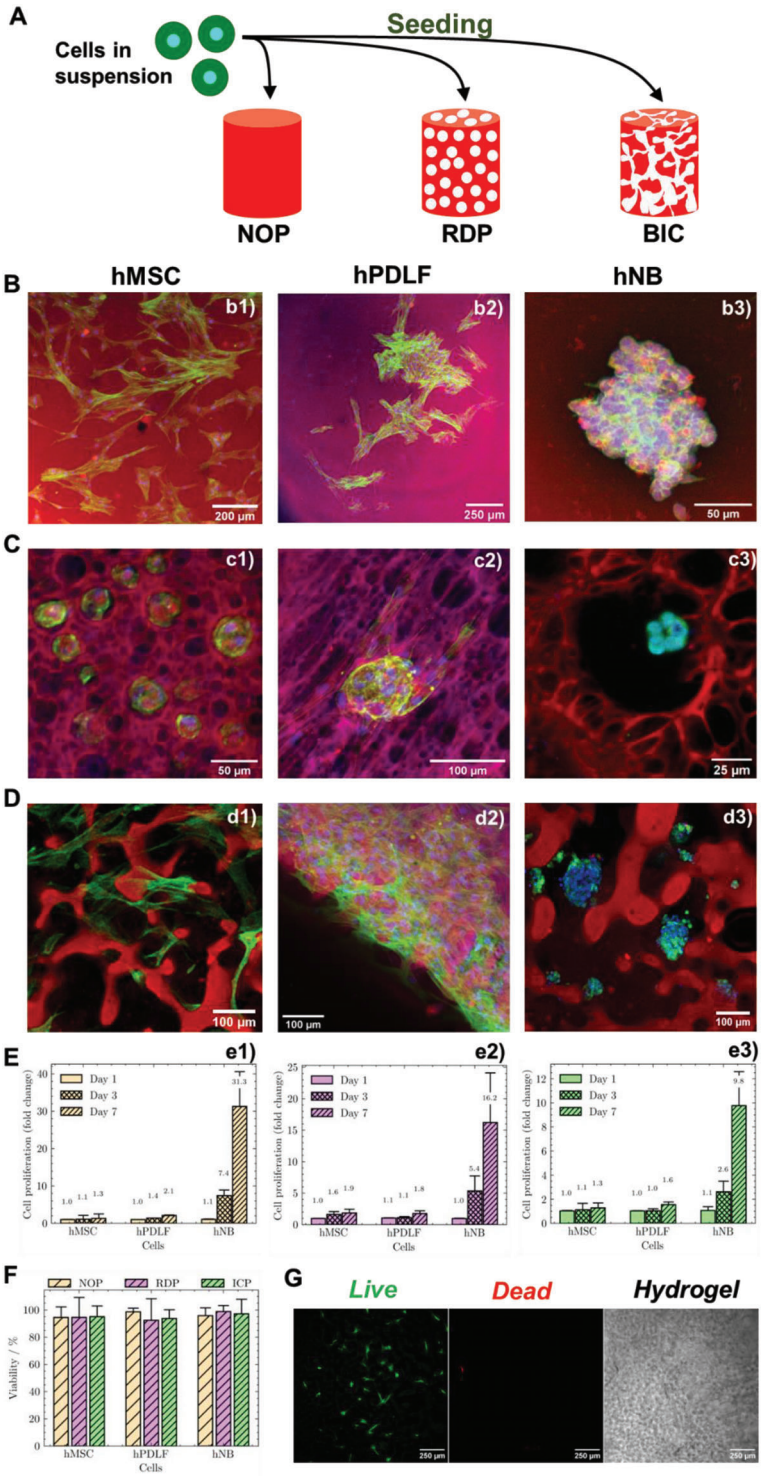

Figure 3. Cell morphology and growth assessments in ATPS hydrogels: A) illustration of cell seeding step in NOP, RDP, and ICP hydrogels; Cell suspensions have been prepared and distributed equally on the top surface of each hydrogel. B–D) Representative images of hMSC, hPDLF, and hNB cell organization B) on top of NOP, and inside C) RDP and D) ICP hydrogels. Phalloidin (green) – F-Actin; DAPI (blue) – nuclear staining; Rhodamine B isothiocyanate (RBITC; red) – ATPS hydrogel. Different scale bars as indicated in the figure offer the best overview of the cell organization and interaction with the specific hydrogel. E) Proliferation of hMSC, hPDLF, and hNB cells in e1) NOP, e2) RDP, and e3) bicontinuous ICP hydrogels. For each cell type, the proliferation rate is determined on days 1, 3, and 7 by a CCK-8 assay and is presented as a mean fold change of the absorbance with respect to day 1 value. F) Viability of hMSC, hPDLF, and hNB cells on day 7 of growth in NOP, RDP, and bicontinuous ICP hydrogels. G) A representative image of the LIVE/DEAD assay indicating alive cells in green and dead cells in red. The brightfield highlights a preserved microstructure of the bicontinuous ICP hydrogels.

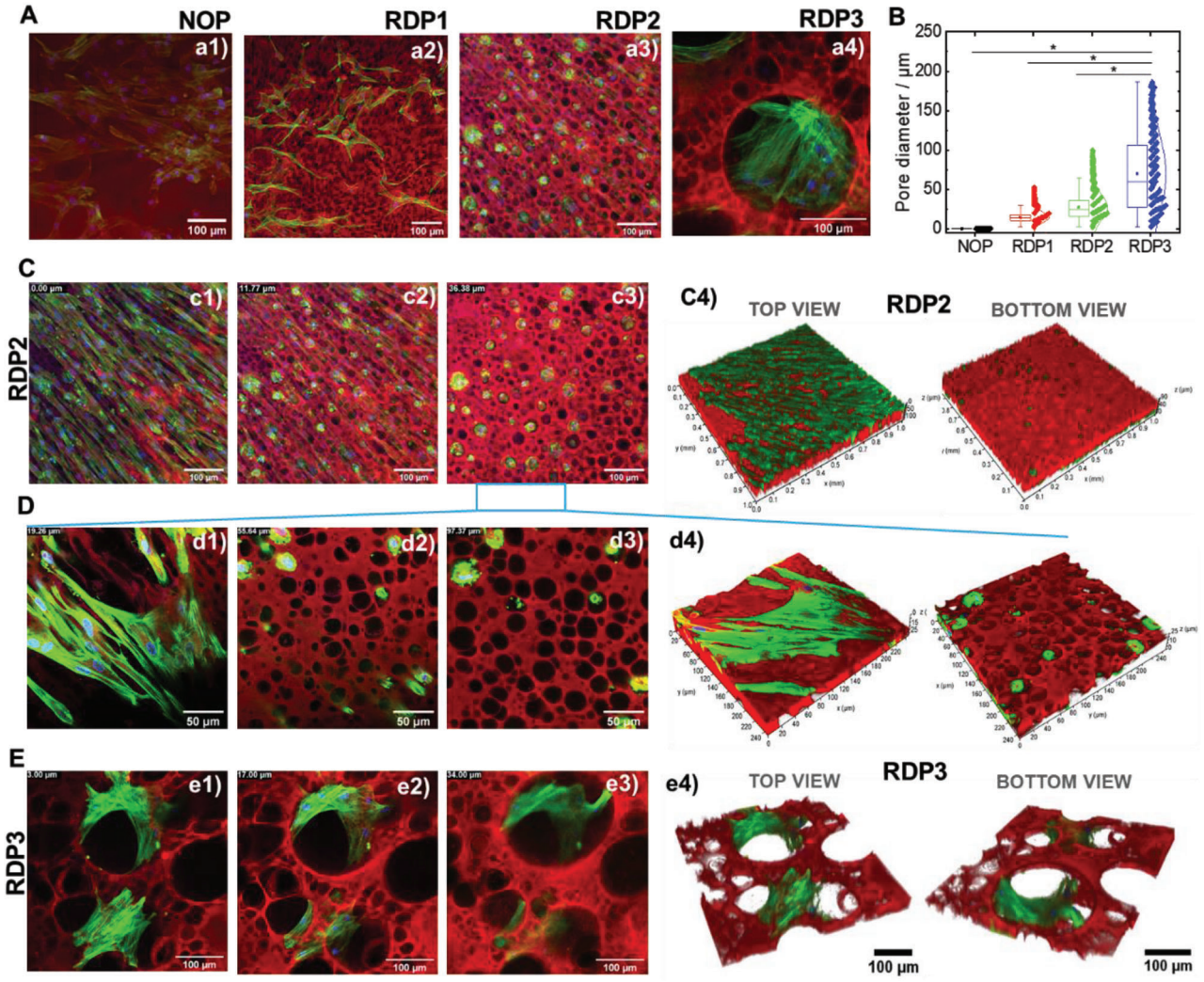

Figure 4. Influence of the pore size of RDP hydrogels on cell distribution during time. A) CLSM micrographs of hMSCs in a1) NOP, a2) RDP1, a3) RDP2 hydrogels, and of hPDLF in a4) RDP3. B) Mean pore size (in µm) of NOP, RDP1, RDP2, and RDP3 hydrogels shown in panel A. *$p < 0.05$. C–E) Organization of hMSC cells at three different depths of RDP2 hydrogel at two different magnifications c1-c3 and d1-d3) and organization of hPDLF cells at three different depths of e1-e3) RDP3. Top left black insets indicate the position of selected Z-projection CLSM micrograph slices for RDP2 (0.0 µm – 11.8 µm – 36.4 µm), at higher magnification (19.3 µm – 55.6 µm – 97.4 µm), and RDP3 (0.0 µm – 17.0 µm – 34.0 µm). The 3D reconstruction of hMSC distribution on the top and bottom surface of c4, d5) RDP2, and e4) RDP3 hydrogels. Phalloidin (green) – F-Actin; DAPI (blue) – nuclear staining; RBITC (red) – ATPS hydrogels. Dimensions of the hydrogel are indicated in µm on the lateral sides of the graphs. Scale bars: 50 and 100 µm.

2.3. Influence of Pore Size on Cell Migration

To explore further the correlation between pore size and cell distribution, we focused on hMSCs and two size-controllable RDP hydrogels (RDP1 and RDP2). NOP is used as a control hydrogel lacking pores at the micrometer scale (**Figure 4**A), while the distribution of hPDLFs, which exhibit behavior in GelMA hydrogels similar to hMSCs, is investigated in RDP3 hydrogels with larger but polydisperse pore size. The preparation conditions of the regular disconnected porous hydrogels is given in [GelMA(mg mL^{-1}) – Dextran(mg mL^{-1}) – HCl(mM)] and are RDP1 [52.8 mg mL^{-1} -10 mg mL^{-1} – 16 mM], RDP2 [52.8 mg mL^{-1} –13 mg mL^{-1} – 16 mM] and RDP3 [52.8 mg mL^{-1} – 15 mg mL^{-1} – 22 mM].

The distribution and spread pattern of cells depend on the microstructure of the hydrogel, and hence the pore dimensions as shown for hMSC (Figure 4a1–a3) and hPDLF (Figure 4a4). The mean pore size of the NOP, RDP1, RDP2, and RDP3 hydrogels is shown in Figure 4B. For the nonporous (NOP) hydrogels, the relevant length scale is given by the average mesh size, which directly indicates the interchain distances. The mesh size of GelMA hydrogel obtained by chemical crosslinking is generally below 200 nm, depending on the GelMA methacrylation degree and physicochemical conditions, i.e., pH, ionic strength, and temperature.[64,65] The mean pore size measured for RDP1, RDP2, and RDP3 was 15, 28, and 70 µm, respectively. Moreover, the pore dimension determined the capacity of hMSCs to migrate to the inside of each of the hydrogels. The dense covering of the top surface of the NOP hydrogel was confirmed with no substantial cell invasion below the hydrogel surface (Figure S5, Supporting Information). In the case of RDP2, hMSC migration

and growth inside the hydrogel were achieved (Figure 4C,D). The behavior of hMSCs on the surface and along the RDP2 hydrogel thickness, shown in Figure S6, Videos S1, and suppinfo3, highlighted the spread of the cells on the hydrogel surface before migrating through the large pores along the hydrogel thickness.

Higher RDP3 hydrogel porosity defined by larger pore size led to better hPDLF cell spreading inside the 3D structure compared to RDP2 (Figure 4E and Figures S7 and S8, Supporting Information). This is also illustrated in Video S3, Supporting Information, highlighting the cells' spread as a function of hydrogel thickness. These findings indicate that cell growth and penetration rate inside GelMA-dextran ATPS hydrogels can be finely tuned while maintaining high cell adhesive affinity to the GelMA polymer and allowing extended cell-to-cell interactions. The former feature is possible due to the presence of the RGD peptides, which assure attractive cell-adhesion sites.[42] To summarize, we determined that pore size can shape the distribution of cells and their spread in 3D hydrogels confirming previous findings.[66]

2.4. Influence of Pore Interconnectivity on Cell Interactions

Although the RDP hydrogels allowed more pronounced cell migration with respect to the NOP hydrogels, it was largely confined due to a lack of pore interconnectivity. However, this limitation was precluded in the ICP hydrogels. The organization of hMSC, hPDLF, and hNB cells in the ICP hydrogels is shown in **Figure 5**. The distribution of the cells along a section of ≈50 µm of the ICP hydrogel thickness was inspected for hMSC (Figure 5A), hPDLF (Figure 5B), and hNB cells (Figure 5C). Selected Z-stack slices investigated by CLSM micrograph from the top and inside the ICP hydrogels highlight that, unlike in the NOP and RDP hydrogels, the cells are distributed throughout the 3D structure mostly without forming a continuous layer on the top surface as highlighted for hMSCs (Figure 5a1–a3), hPDLFs (Figure 5b1–b3) and hNBs (Figure 5c1–c3).

The analysis of the mean fluorescence intensity of each of the analyzed channels (DAPI-blue, phalloidin-green, and RBITC-red) as a function of the hydrogel thickness also excluded eventual interruptions in cell distribution within the hydrogel (Figure 5a4,b4,c4). More precisely, it confirmed that the cell-originating fluorescence (nuclei (blue signal) and F-actin (green signal)) was continuously detected through the interconnections of the hydrogel and that it was properly aligned with the hydrogel-deriving fluorescent signal (Figure 5a1-a3,b1-b3,c1-c3). The 3D reconstructions of the Z-stacks' projections for hMSC, hPDLF, and hNB cells in ICP hydrogels are shown in Figure 5a5,b5,c5, respectively. The meshwork-like pattern of cell organization and distribution along the ICP hydrogels' thickness was demonstrated for hMSCs and hPDLFs, as also shown in Video S4, Supporting Information for the latter. In contrast, hNB cells grew in clusters, as shown from separated and merged channels in Figure S9 and Video S5, Supporting Information. This different distribution of the cells with diverse phenotypes emphasizes that the ICP hydrogel preserves specific (patho)physiological functions of the cells as shown for hMSC cells in Figure S10, Supporting Information. Finally, ICP also allowed a co-culture of hPDLF and EC cells leading to complex 3D cell organizations and interactions. This is shown in Figure 5D in the separated channels and their merging (Figure 5d1–d4 and Figure S11, Supporting Information) as well as along the hydrogel thickness from the 3D construction (Figure 5d5, Figure S12, and Video S6, Supporting Information). The latter result supports the use of ICP hydrogel as a versatile material for investigating a broad range of cellular interactions essential for defining specific biological functions.[67]

2.5. Printability of GelMA-Dextran ATPS Hydrogels

The key to preparing ATPS hydrogel with tunable microstructure is to control the competition between the phase separation and gelation kinetics. This control becomes even more challenging when hydrogels are fabricated by manufacturing techniques like 3D printing. The printing step requires additional time, and applies shear stress which could affect the phase-separation process or the structure and size of the phase-separated domains. While the gelation kinetics can be controlled by adjusting the photocrosslinking conditions leading to gelation in a few seconds, the phase separation kinetics is crucial. It should be slow enough (minutes scale) to allow sufficient time to enable reproducing the microstructure of the hydrogels.

Prior to 3D printing experiments, we assessed the influence of pH and temperature on the phase separation kinetic. Selecting a pH 4.9 on the onset of the turbidity curve, (please refer to the turbidimetric curves titration in Figure 1C), the system remains relatively turbid with no notable macroscopic phase separation for at least 30 minutes. In contrast at pH 4.5, i.e., high turbidity, the phase separation is very fast with a macroscopic phase separation within less than 5 min. Although the pH-dependent phase separation is beyond the scope of the current work, it may be related to the GelMA behavior in solution as a function of pH. Adjusting the pH near the isoelectric point of GelMA, results in a decrease of electrostatic repulsions between intra- and inter-chains and therefore favors the self-association of GelMA molecules and which can accelerate phase separation.

Next, we investigated the influence of temperature at pH 4.9. At 37°C, the GelMA-dextran mixtures remained slightly turbid without visible macrophase separation for at least 30 min. The influence of decreasing temperature on the phase separation kinetic was investigated. Surprisingly, the phase separation at 27 °C, is faster than at 37 °C with the formation of two distinct phases in less than 10 min. This observation is probably related to the structural transition of GelMA molecules from the coil to triple helix during cooling below 30 °C.[68,69] Thus, increasing the excluded volume effect and, therefore, the entropy of mixing results in an accelerated phase separation process.[68,69]

The inkjet 3D printing process was optimized following the investigation of the influence of the valve diameter, the applied pressure and the used surface as a printing platform by measuring the contact angle of the GelMA-Dextran ATPS (Figure S13, Supporting Information).

For inkjet 3D printing, a shear-thinning fluid with a low shear viscosity is required. **Figure 6**A shows the shear viscosity as a function of shear rate at 37 °C of homogenous, dextran droplets in GelMA continuous phase and the bicontinuous system. The homogenous system demonstrates a Newtonian behavior, while, the dextran droplets dispersed in GelMA phase and bicontinuous systems exhibited a shear-thinning behavior.

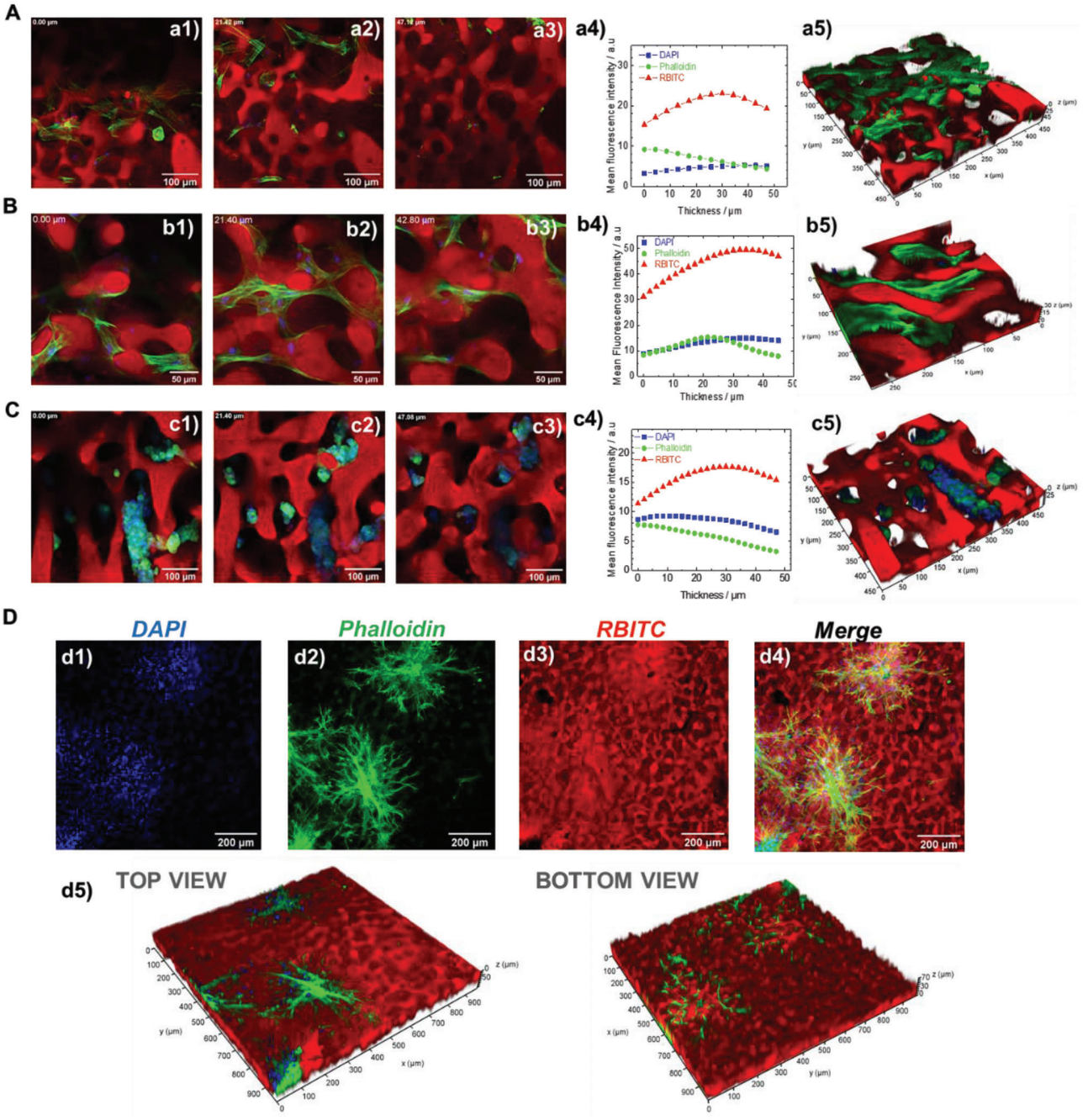

Figure 5. Cell distribution in ICP hydrogels. Distribution of A) hMSC, B) hPDLF, and C) hNB cells inside the ICP hydrogel. a1-a3), b1-b3), and c1-c3) Selected Z-stack slices. The top left numbers mark the depth of the selected Z-slice. A total thickness of about 50 µm was considered. a4), b4), and c4) Evolution of mean DAPI (blue), phalloidin (green), and RBITC (red) dyes mean fluorescence intensity as a function of hydrogel thickness section for hMSC, hPDLF, and hNB cells, respectively. a5), b5), and c5) the 3D reconstruction images for hMSC, hPDLF, and hNB cells distribution, respectively. D) Co-culture of hPDLF and endothelial (hEC) cells in ICP hydrogels. Diffuse cell network is achieved after 7 days of hPDLF and hEC co-culturing. Separated channels d1) DAPI, d2) phalloidin, d3) RBITC, and d4) the merged channels d5). The 3D reconstruction of co-cultured cell distribution on the top and bottom surface of ICP hydrogel. Dimensions of the hydrogel are indicated in µm on the lateral sides of the graphs. Scale bars: 50, 100, and 200 µm.

The CLSM 3D construction images of the printed hydrogels reveal that the microstructures of the RDP and ICP hydrogels are similar to the casted hydrogels (Figure 6B,C). That shows that the applied shear stress during the printing step did not affect the initial microstructure. ICP hydrogels were printed at pH4.9 and pH4.7 and their microstructure is shown in Figure 6D,E. Decreasing the pH results in an increase of the pore size distribution (Figure 6F). By varying the pH of the ATPS, it was possible to print ICP hydrogels with an increased characteristic length scale (Figure 6G). Additional CLSM images of printed ICP hydrogels

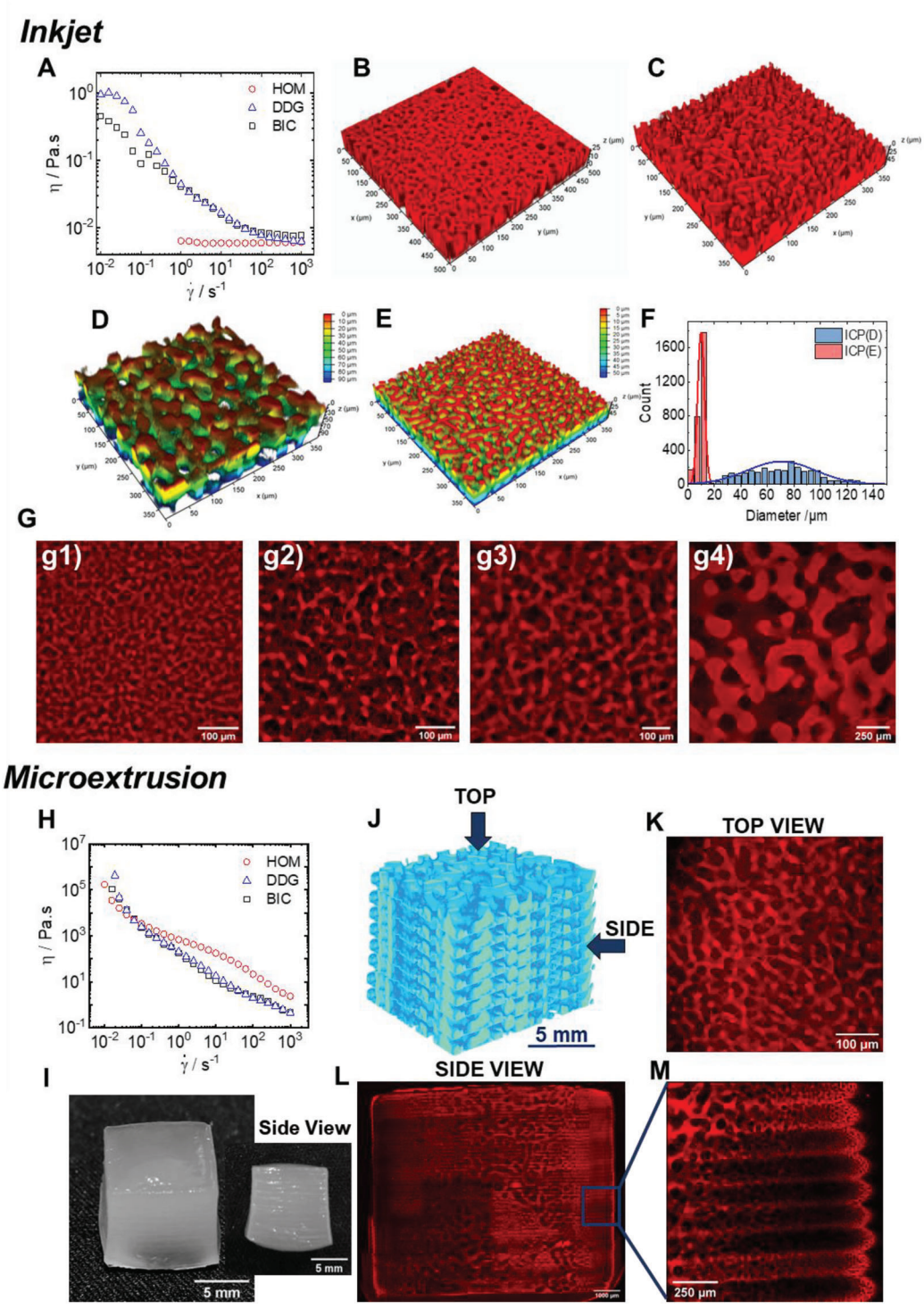

Figure 6. 3D printing of ATPS hydrogels by inkjet (A–G) and microextrusion (H-M). A) Viscosity as a function of shear rate at 37 °C. Typical CLSM 3D construction of printed RDP (B) and ICP (C) hydrogels. Typical CLSM 3D construction with depth coding of ICP hydrogels with different length scales, printed from a bicontinuous solution at pH4.7 (D) and 4.9 (E) and (F) the pore size distribution ICP(D) and ICP(E), respectively. The bin size is 5 μm. G) Printed ICP hydrogels with increasing characteristic length scale at g1) pH 5, g2) pH 4.9; g3) pH 4.85, and g4) at pH 4.7 after complete phase separation followed by remixing. Scale bars are 100 μm (g1-g3) and 250 μm (g4). H) Viscosity as a function of shear rate at 4 °C. I) Photograph of the swollen printed cubic multilayered hydrogel. J) Illustrative 3D model of multilayered hydrogel printed by microextrusion. K) CLSM image of a section from the top view of the multilayered hydrogel. L) CLSM micrograph of the multilayered hydrogel obtained by a mosaic merge of tile scan images and M) high magnification of hydrogel edge from image *K* highlighting the layered hydrogel structure. Dimensions of the hydrogel are indicated in μm on the lateral sides of the graphs. The HOM, DDG, and BIC abbreviations in the legend panels of A and G refer to the homogenous mixture, dextran droplets dispersed in GelMA phase, and bicontinuous mixture, respectively.

via inkjet printing are shown in Figure S14, Supporting Information.

Moreover, multilayered ICP hydrogels were manufactured via microextrusion-based 3D printing. Microextrusion of hydrogels with high resolution requires inks with higher viscosities than inkjet techniques. To avoid the addition of a viscosity modifier, increasing ATPS viscosity was achieved through the physical gelation of GelMA at 4 °C. The gelation occurs by GelMA transition from coil to triple helix and the formation of ordered helical collagen-like sequences separated along the GelMA molecular contour by peptide residues in the disordered coil conformation.[70] Since the gelation kinetics may significantly affect the resulting hydrogel microstructure, the influence of the cooling rate on the resulting ICP microstructure was investigated beforehand, as shown in Figure S15, Supporting Information. The typical CLSM images of the different samples are shown in Figure S15C, Supporting Information and demonstrate that only a very fast quench at 4 °C preserves the bicontinuous structure (Figure S15A, Supporting Information), while slower cooling in situ in the rheometer (Figure S15B, Supporting Information) lead to heterogeneous microstructure and favor the appearance of droplets and, therefore, of RDP physical hydrogel formation.

Viscosity as a function of shear of the rapidly cooled system was measured at 4 °C (Figure 6H). The flow curves highlighted the highly viscous samples with viscosities greater than 10^5 Pa.s at lower shear rates and with a pronounced shear thinning. Based on this observation, a fast-quenched bicontinuous ATPS GelMA-dextran mixture at 4 °C, was printed by microextrusion (Figure 6I). A 3D illustration of the printed multilayered hydrogel is shown in Figure 6J. The CLSM top view image highlights the preserved bicontinuous structure (Figure 6K), while a tile scan followed by a mosaic merge along the hydrogel thickness highlights the hierarchical structure and formed layers as shown in Figure 6L and the magnified Figure 6M. Although the global multilayered hydrogel may exhibit pores discontinuities from one layer to the next, the preparation of such a hierarchical structure could be used to compartmentalize the hydrogel for the growth of different cell lines or to encapsulate active molecules. The three different ATPS hydrogels, NOP, RDP, and bicontinuous ICP, with different length scales, were successfully printed with inkjet and microextrusion 3D printing methods.

3. Discussion

The quest for functional hydrogels with controlled features and microstructure is challenging. For many applications, and in particular, in the field of tissue engineering, control of the pore size and interconnectivity are essential in order keep embedded cells alive over longer cultivation periods. While many approaches for the generation of porous hydrogels were reported,[5,6,16] the use of aqueous two-phase system (ATPS) is a straightforward approach.[24] The development of porous hydrogels from ATPS is based on gelling one phase during phase separation, while the second phase is used as a sacrificial template.[24] Technically, synthesizing a randomly porous hydrogel from ATPS is feasible;[24] however, controlling the pore structure and organization and the final microstructure of the hydrogel remains challenging.[35] The main challenge is to control i) the phase separation mechanism and ii) the competition between phase separation and gelation kinetics of the out-of-equilibrium ATPS. Controlling the gelation kinetic is relatively straightforward, especially for photocrosslinkable polymers like GelMA. The gelation kinetic can be fast within seconds and is controlled by the photoinitiator concentration, UV intensity, and exposure time. In contrast, controlling the phase separation process is more challenging and requires understanding the influence of the physicochemical parameters on the phase separation mechanism and kinetics.

Previous studies reporting porous ATPS-based GelMA hydrogel used polyethylene oxide, [13,34,35] polyethylene glycol,[71] polyvinyl alcohol,[35] and dextran[35] as a sacrificial template. The segregative phase separation was induced in phosphate-buffered saline (PBS) buffer.[13,34,35,71] The influence of temperature and concentration of GelMA and the used polymer to induce phase separation was investigated. The influence of the methacrylation degree of GelMA and molecular weight of polyethylene oxide, polyvinyl alcohol, and dextran was also investigated.[35]

While highly (micro)porous hydrogels were obtained,[35] these studies highlighted how developing bicontinuous hydrogels in saline conditions is challenging.[13,34] The systems discussed above as well as our system consist of a polyampholyte (GelMA) and a neutral polymer (such as dextran, polyethylene glycol, polyethylene oxide, or polyvinyl alcohol). In this type of mixture, phase separation is promoted when the charge density of the polyampholyte is decreased.[45,46,72] This can be achieved either by screening the charges of the polyampholyte by adding salt, like in the previous studies using PBS buffer, or by adjusting the pH in salt-free conditions to affect the protonation/deprotonation of the functional groups. We selected the latter approach, and we investigated the phase separation process of the GelMA/dextran system as a function of pH and concentration of dextran. Our experimental approach consisted of determining the isoelectric point (IEP) and evaluating the charge density dependence of GelMA as a function of the pH. The IEP of GelMA is between pH 4.1 and 4.4 and is significantly lower than the IEP of the native gelatin (between 7 and 9).[48] The acidification of a monophasic system of GelMA-dextran from neutral to low pH, demonstrates the pH-dependent stability and the occurrence of phase separation during acidification around the IEP of GelMA. The stability of the system as a function of the charge density of GelMA is in good agreement with previous fundamental studies on the phase behavior of nongelling gelatin-dextran which demonstrated a shift of the binodal, i.e., delimiting line separating monophasic and biphasic region, as a function of pH and salt.[45,46,72] We also observed that the phase separation kinetic is slower at pH 4.9 than at pH 4.7. Slowing the phase separation of ATPS solution is of great importance in developing GelMA hydrogels with reproducible microstructure.

Porous hydrogels composed of regular pores and their applications as biomaterials are widely reported.[6,24] Very recently, GelMA hydrogels with a high density of connected micropores were reported by using polyvinyl alcohol, polyethylene oxide, or dextran as a sacrificial template.[35] In the current study, we also demonstrate the possibility of preparing GelMA hydrogels with high density of dispersed pores by either adjusting the pH and varying the dextran concentration (Figure 1D,E) or by the addition of an increasing amount of NaCl (Figure S3d, Supporting Information). While the development of hydrogel derived

from ATPS, with dispersed pores is actively reported, the development of bicontinuous hydrogels with interconnected pores is still scarce.[13,25,34,71] One of the main reasons is the thermodynamic instability of bicontinuous which arises from spinodal decomposition. Therefore, developing bicontinuous hydrogels implies understanding the main parameters affecting the phase separation mechanism and kinetics.

Previous bicontinuous GelMA hydrogels were therefore obtained by adjusting the concentrations of GelMA and, polyethylene oxide (PEO) or polyethylene glycol (PEG), and clearly demonstrated how challenging obtaining a bicontinuous structure is.[13,34,71] One common point between the experimental approaches in these studies is that the ATPS of GelMA-PEO and GelMA-PEG were prepared in a PBS buffer.[13,34,71] In contrast to previous studies, we were able to prepare hydrogels with a reproducible bicontinuous microstructure by controlling the pH. As mentioned earlier, the phase separation kinetic is pH-dependent, i.e., slower at pH 4.9 than at pH 4.7 and pH 4.5 which are close to the IEP of GelMA. Furthermore, the pH variation allows to control the characteristic length scales of the pores of the bicontinuous hydrogels. We believe that the challenging point in the previous studies is due to the use of salt (PBS buffer) to induce segregative phase separation. For this reason, we have tested the effect of NaCl on GelMA-dextran system. We found that the system turns more to dextran droplets dispersed in the GelMA phase rather than to a bicontinuous system.

While at first glance, both pH (decreasing the charge density of GelMA) and salt (screening the charges of GelMA) promote phase separation, the influence of salt seems more complex than pH. The addition of salt can either affect the phase separation mechanism (from spinodal decomposition to nucleation and growth) or act on the early stage of spinodal decomposition by stabilizing the water–water interface leading to the formation of droplets via a percolation-to-cluster transition. Even though further investigation is required, the latter hypothesis is conceivable since it was previously shown that the salt decreases the already low water–water interfacial tension.[46,73]

Next, we studied the behavior of seeded cells along the hydrogel thickness for the gels with different microstructures. The influence of the size of disconnected pores demonstrates that a minimum mean pore size of 27 μm is required to induce hMSC migration and growth inside the hydrogel. The CLSM examination along the hydrogel thickness revealed that the cells first spread on the surface of the hydrogel before migrating through the large pores. Higher hydrogel porosity, with a mean pore size of 70 μm, led to better hPDLF cell spreading inside the 3D structure. This is in good agreement with a similar previous study based on the static seeding of human skin fibroblast cells on porous chitosan hydrogels prepared by CO_2 bubbling.[74] Comparable, in our 3D system, an optimal cell spreading was detected on the surface of the RDP hydrogels and was sustained by cell penetration inside the pores after 7 days. This result confirms proadhesive features of the GelMA surface in our ATPS which is in good agreement with a previous study on GelMA nonporous hydrogel that explored adhesion, proliferation, and migration of phenotipically similar cell types.[75] However, since the cell behavior depends on the characteristics of the polymer, it is importance to highlight the difference in pro-adhesive nature between GelMA and chitosan. While GelMA provides integrin-binding RGD (Arg-Gly-Asp) motifs and metalloprotease digestion sites that favor cell attachment,[42] chitosan lacks the adhesion motifs that are recognizable by the cells.[76] This property is determinant in defining the strength of cell-to-polymer interactions and hence the cell spreading pattern through the pores.

Next, we investigated the influence of bicontinuous structure and therefore the interconnectivity of the pores of ICP hydrogels on the cell behavior. CLSM performed from the top and inside the ICP hydrogels highlight that the cells are distributed throughout the 3D structure. A simultaneous observation of cells and hydrogel by CLSM allowed the comprehension of both, cell-to-cell interaction and cell distribution with respect to the hydrogel microstructure. This is of great importance in understanding the behavior of cells in pore communicating hydrogels. For instance, up-to-date, confocal studies reporting the development of bicontinuous GelMA hydrogels are very limited. They presented only the cells organization and, therefore cell-to-cell interaction, without giving a clear imaging on how the cells interact with the adjacent hydrogel surface.[13,34,71] Indeed, visualization of both, interconnected pores and biological material, was until now only available for interconnected porous PEG hydrogel and cluster neurons, resulting in functional, highly viable, and long-term stable 3D neural networks in the synthetic ECM.[25]

In this study, we explored the behavior of three functionally different human cell types namely, hMSCs, hPDLFs, and hNBs demonstrating a diversity in their organization patterns. While hMSCs and hPDLFs defined a meshwork-like network, hNBs cells preferentially grew in clusters even if communicating pores are provided. This finding is crucial since highlighting that the behavior of each cell type depends primarily on their biological background and function and then on hydrogel characteristics.

The 3D-printing of the bicontinuous system was previously achieved by printing a physical bicontinuous gel at 15 °C.[13,34] Herein, we demonstrated the possibility to print both bicontinuous solution at 37 °C (Figure 6C–G) by inkjet printing and bicontinuous gel at 4 °C by microextrusion (Figure 6H–M). This leads to great flexibility in terms of printing temperature, technique, and bicontinuous state (solution or gel). Moreover, by varying the pH, we demonstrate for the first time the possibility of printing bicontinuous solutions with different length scales of pores (Figure 6C–G). The preserved microstructure allowed us to design, a multilayered bicontinuous hydrogel (Figure 6J–M) which could be useful for creating complex, cell-containing, multi-compartment systems applicable in numerous bioengineering fields requiring cell-responsive engineered hydrogels.

4. Conclusions

We have demonstrated that the pH-dependent segregative phase separation of GelMA- dextran aqueous two-phase system, results in hydrogels with reproducible and controllable microstructures. By adjusting the pH and dextran concentration, we successfully developed GelMA hydrogels with three distinct microstructures, namely Nonporous (NOP), Regular Disconnected-Pores (RDP), and bicontinuous Interconnected-Pores (ICP). The length scale of pores of the bicontinuous hydrogel can be controlled by fine-tuning the pH and dextran concentration, ensuring high reproducibility of the microstructure. To the best of our knowledge, such reproducibility and control of the pore length scale of bi-

continuous structures for biomaterials applications were not reported so far. The three types of hydrogels were suitable for growing phenotypically different cell types that all maintained optimal viability and expected morphology after seven days of culture. The bicontinuous ICP hydrogels showed the most promising features in sustaining cell distribution throughout the hydrogel even in a condition of a co-culture of two different cells types. Finally, we demonstrated the possibility of 3D print both bicontinuous solutions as well as bicontinuous gels with a tailorable length scale of pores.

5. Experimental Section

Chemicals: Gelatin (type A, 300 bloom from porcine skin, lot # SLCD2367), dextran (450–650 KDa) from Leuconostoc spp., (lot #BCCC3405), Rhodamine B isothiocyanate, methacrylic anhydride (MAA), the photoinitiator 2-hydroxy-4'-(2-hydroxyethoxy)−2-methylpropiophenone (Irgacure 2959), phosphate buffer saline (PBS) tablets, and sodium chloride (NaCl) were purchased from Sigma-Aldrich (Germany).

GelMA Synthesis: The GelMA-modified protein was synthesized by reacting the native gelatin with MAA according to the protocol developed by Lee et al.[77] Briefly, gelatin was dissolved at 10% w/v at 60 °C in PBS buffer. GelMA was prepared by reacting the free amino and hydroxyl groups of gelatin with MA at 0.1 mL per gram of gelatin at 50 °C for 3 h. One-sixth of 1 mL MAA was added to the gelatin solutions every 30 min for 3 h in a dropwise format. After each MAA addition, the pH was adjusted back to 7.4–8.2 with sodium hydroxide (NaOH 5 M) since the gelatin-MAA reaction results in methacrylic acid formation in the solution. The chemical reaction was illustrated in Figure S16a, Supporting Information.

The reacted gelatin was purified by dialysis to remove salt and methacrylic acid. The synthesized GelMA was purified by dialysis, then freeze-dried and stored at 4 °C until use.

^{1}H-NMR: The ^{1}H-NMR spectra of native gelatin and GelMA were recorded in D_2O on an AV300 MHz NMR (Bruker BioSpin, USA) at 40 °C. Chemical shifts were given in ppm relative to the residual solvent peak. The degree of methacrylation, determined by ^{1}H NMR, is 75% (Figure S16b, Supporting Information).

Determination of GelMA Isoelectric Point (IEP): The GelMA IEP was determined by measuring the electrophoretic mobility of GelMA 0.05 mg mL^{-1} solution as a function of pH in the pH 7–2 range. The pH autotitration measurements were conducted using an MPT-3 multipurpose autotitrator and a Zetasizer Ultra (Malvern Instruments Ltd., Malvern, UK). The measurements were acquired in a DTS1070 capillary cell. For each pH value, 3 measurements were made with a maximum of 30 runs per measurement and a 60 s pause between each repeated measurement. All titrations were achieved using 0.1 M and 0.01 M HCl and conducted at 37 ± 0.1 °C.

Preparation of ATPS Solutions: The modified protein solution was prepared by dispersing the GelMA foam and the photoinitiator in water at final concentrations of 100 and 10 mg mL^{-1}, respectively. The solution was heated at 60 °C under stirring until its complete solubilization. Dextran solution (140 mg mL^{-1}) was prepared in water under stirring at room temperature (RT). The prepared GelMA and dextran solutions, HCl 0.1 M, and H_2O were incubated at 37 °C. The ATPS mixture was then prepared by mixing a specific volume of dextran, HCl 0.1 M, and H_2O and, finally, by adding the GelMA solutions. The homogenous GelMA-dextran mixture leading to non-phase-separated hydrogels was prepared by mixing GelMA-dextran and H_2O. The final composition of the mixtures is expressed as [GelMA (mg/mL), Dextran (mg mL^{-1}), HCl (mM)]. Dextran droplets dispersed in GelMA continuous phase [52.8 mg mL^{-1}, 12.3 mg mL^{-1}, 20 mM] and bicontinuous system [52.8 mg mL^{-1}, 24.6 mg mL^{-1}, 9 mM] model systems were prepared and, following the gelation step and dextran washing out, led to regular disconnected porous (RDP) and bicontinuous interconnected porous (ICP) hydrogels, respectively. The influence of HCl molarity and dextran concentrations on the model systems and final hydrogels microstructure was investigated. Nonporous (NOP) hydrogels resulted from the photo-crosslinking of a homogenous monophasic GelMA/dextran mixture [52.8 mg mL^{-1}−12.3 mg mL^{-1}, 0 mM] in water (pH 6.5). It should be noted that nonporous refers to the absence of micropores; therefore, the network mesh size governs the porosity of the hydrogel.

UV-Vis Spectrophotometry: The influence of pH on the segregative phase separation was investigated by measuring the absorbance at a wavelength range of 400–700 nm. GelMA-dextran ATPS mixtures of 52.8 mg mL^{-1} – 12.3 mg mL^{-1} and 52.8 mg mL^{-1} – 24.6 mg mL^{-1} were prepared in water. The mixtures were homogenous, and the solutions were clear. The influence of the acidification was then investigated by adding HCl 0.1 M dropwise at 37 °C under stirring. After each addition, the pH was measured, and the mixture was vortexed and transferred into a cuvette to measure the absorbance. The turbidity was then reported as 100 − %T (where T is the transmittance and is equal to 10^{-A} and A is the absorbance at 600 nm). Data were recorded at 37 °C using a UV/Vis spectrophotometer Cary 100 Bio (Agilent Technologies, USA).

Hydrogel Preparation: ATPS-based hydrogels were prepared by either casting in a multiwell plate or by inkjet 3D printing.

Hydrogel Preparation—Casting: ATPS-based hydrogels were prepared in a 96 multiwell plate. The solutions were vortexed before pouring 55 µL into each well. The samples were photo-crosslinked using a UV LED lamp (30-W, 365 nm) for 4 min, then 200 µL of water was added on the top of each hydrogel and the samples were stored at 4 °C in the dark until further use. For cell seeding experiments, the hydrogels were washed twice and transferred into physiological water (NaCl 0.9%).

Hydrogel Preparation—3D Printing: The printing experiments of ATPS solutions were performed using a custom-built air pressure-driven printer as previously described.[78,79] The printer comprised two microvalve-based (Fritz Gyger, Gwatt, and Switzerland) print heads, each individually controllable and heatable, mounted to a three-axis robotic system (Isel, Eichenzell, and Germany). The print head carrying the ATPS solution was heated to 37 °C, and the printing pressure was set to 0.05 bar. In this part, several parameters namely were varied, the needle size (ID 0.1, ID 0.51, and ID 0.8), the extrusion pressure (0.1, 0.2, and 0.4 bar). It was observed that nicely shaped strands are formed with ID 0.8 and ID 0.5 needles, while droplets were formed with needle ID 0.1. For inkjet printing, a microvalve with a diameter of 450 µm and opening times of 450 µs was used, and 1000 drops were deposited. This allowed for a reliable and reproducible droplet deposition. Further inkjet printing characterizations and contact angle measurements were also conducted. For microextrusion, the precooled hydrogel was processed with a 25-gauge needle by applying 0.8 bar. The hydrogel was cooled during the printing by a custom-built extrusion housing. Petri dishes were used as a printing platform. The printed samples were cured with a UV LED lamp (30 Watts, 365 nm). The printing process was controlled using a software platform developed in-house.

Mechanical Characterization: The mechanical properties of the NOP, RDP, and bicontinuous ICP hydrogels were investigated using a Discovery Hybrid Rheometer (DHR3, TA instruments, USA) equipped with a force transducer of 50 N and a plate geometry of 20 mm diameter. Cylindrical hydrogels 6 mm in diameter and 6 mm in height were prepared by pouring 200 µL of ATPS solution in wells of a 96 multiwell plate, followed by UV photo-crosslinking for 4 min using a UV lamp. Subsequently, the hydrogel discs were incubated in water overnight to achieve swollen equilibrium before conducting the compression experiments. The hydrogels were then compressed along with the height, from 6 to 1 mm, with a linear compression speed of 1.2 mm min^{-1}. The gap (l) and the normal force (F) imposed were measured simultaneously at the upper plate. The force-displacement responses were re-plotted in terms of stress (σ) and strain (ϵ), with $\epsilon = (l_0 - l\,/l_0)$, where $l_0(m)$ is the original height of the hydrogels, and l (m) is the current height during compression; $\sigma(kPa) = F/A*1000$, where A (m^2) is the cross-sectional area of the hydrogels.

Rheology: Rheological characterization of the ATPS solutions and hydrogels was conducted using a Discovery Hybrid Rheometer HR 3 (TA Instruments, USA).

Rheology—Shear Viscosity: The steady-shear viscosity of ATPS solutions was determined using a cone-and-plate geometry (diameter 40 mm,

angle 1.986°, and truncation 57 µm) by increasing the shear rate ($\dot{\gamma}$) from 10^{-2} to $10^{3} s^{-1}$. The experiments were conducted at 37 °C using the Peltier temperature system, which allows accurate temperature control by the stainless-steel lower plate and a solvent trap to ensure minimal water evaporation during the measurements.

Rheology—Oscillatory Rheology: These experiments were performed using a stainless-steel upper plate (diameter 20 mm) coupled with a UV-curing accessory lower part (Figure S17, Supporting Information). During the experiments, an imposed axial force ($F = 0.1\ N$) with an initial gap ($h = 0.5$ mm) was applied. The GelMA-dextran solutions were prepared at 37 °C, vortexed, and poured immediately onto the quartz lower plate geometry surface.

To monitor ATPS gelation, the elastic (*G*') and viscous (*G*'') moduli were recorded using a $f = 1\ Hz$ and a strain ($\gamma = 5\%$). The selected strain value was previously confirmed to be within the linear viscoelastic regime (LVER) after conducting a dynamic strain sweep at a frequency (F = 1 Hz) by varying the shear strain (γ) from 0.01 to 100%. After complete UV curing where *G*' and *G*'' reached a plateau, a frequency sweep test was conducted by varying the frequency between 10 and 0.01 Hz using a strain of 5% with the LVER.

To study the influence of the cooling rate on the resulting ICP hydrogel microstructure, bicontinuous solutions were prepared at 37 °C and immediately poured on the rheometer coupled with a Peltier system and preheated at 37 °C. Physical ICP gelation was monitored at different cooling rates (0.5, 1, 2.5, and 10 °C) from 37 to 4 °C. Gelation in situ was followed by a frequency-time sweep and monitoring G' (t) and G'' (t) during cooling at a frequency $f = 1$ Hz and a strain ($\gamma = 5\%$). Afterward, the resulting physical hydrogels were crosslinked by applying a UV light using an external UV LED lamp and observed using CLSM. For very fast or instantaneous physical gelation, a GelMA-dextran bicontinuous solution was transferred into a pre-cooled tube in an ice bath, leading to very fast physical gelation before UV photo-crosslinking.

Cell Lines and Primary Cells: Human cell line SH-SY5Y derived from hNB bone marrow metastatic disease was purchased from the Deutsche Sammlung von Mikroorganismen und Zellkulturen (DSMZ; ACC 209) and human periodontal ligament fibroblast (hPDLF) from Lonza (CC-7049 Lonza). The hNB cell line was cultured in Dulbecco's Modified Eagle Medium (DMEM) supplemented with 10% FCS and 100 U mL^{-1} penicillin/streptomycin (all from PAN Biotech, Aidenbach). The hPDLF was grown in DMEM (high glucose; 4.5 g/l D-Glucose, L-Glutamine) supplemented with 10% FBS, 100 U mL^{-1} penicillin/streptomycin, and 50 mg L^{-1} of Ascorbic acid (Sigma–Aldrich, Germany). Human primary bone marrow-derived multipotent primary mesenchymal stromal cells (hMSCs) were isolated as previously described.[80] The use of hMSCs was approved by the local ethic committee (EK 300/14). The hECs were isolated from the umbilical vein after processing with 1 mg mL^{-1} of type II collagenase for 30 min at 37 °C (Thermo Fisher). Cells were seeded in the flasks precoated with 2% of sterilized gelatin (Sigma) and expanded in the endothelial basal medium enriched with the EGM-2 growth supplements (PromoCell, Heidelberg, Germany). The use of hECs was approved by the local ethics committee (EK 424/19). The primary cells were cultured until the 5th passage. For cell experiments, 3D hydrogel structures were prepared by casting and 3D printing approaches. Cells, prepared as pellets and diluted in the corresponding cell medium, were distributed equally on the surface of hydrogels and left for 30 minutes to diffuse inside each hydrogel before completely covering the hydrogel with the additional medium. For cell labeling, phalloidin and diamidino-2-phenylindole (DAPI) were used for F-actin and nuclei staining, respectively. Confocal Laser Scanning Microscopy (CLSM) experiments demonstrated that each cell type maintained optimal viability and expected morphology after 7 days of culture.

Cell Proliferation and Viability Assessment: The Cell Counting Kit-8 (CCK-8, Dojindo Laboratories, Kumamoto, Japan) assay was performed to monitor cell proliferation rate following the manufacturer's recommendations. Briefly, the same samples were incubated for 3 h at 37 °C on days 1, 3, and 7 in 1 mL of medium containing 100 µl of CCK-8 solution per sample. In the following, 3 × 100 µL of culture media were transferred into 96-well culture plate and sample's absorbance was detected at 450 nm using a microplate reader (Sectramax M2, Molecular devices, San José, USA). The results are presented as a proliferation fold change calculated with respect to day 1 of each experimental condition. Cell viability was analyzed after 7 days of in vitro growth using LIVE/DEAD™ two-color assay (Thermo Fisher) following the protocol suggested by the manufacturer. The incubation was done for 3 h at 37 °C and samples were analyzed by confocal laser scanning microscopy (CLSM) in the following.

Confocal Laser Scanning Microscopy (CLSM): CLSM was performed with a LeicaSP8 Tandem Confocal system (Leica Microsystems GmbH, Germany). Samples were excited with the dye's specific wavelength, and the emission was detected using photomultiplier tube (PMT) and hybrid detectors (HyD). CLSM images were analyzed using FIJI software (Fiji Is Just ImageJ), and 3D construction from Z-stacks was performed using the 3D visualization module of the Leica Application Suite X (LAS X) software. The pores distribution of the RDP and ICP hydrogels was measured using Aquami, an automated image analysis software written in Python programming language.[81]

Scanning Electron Microscopy (SEM): SEM experiments were performed in a high vacuum environment by 10 kV accelerating voltage Environmental Scanning Electron Microscopy (ESEM XL30 FEG, FEI, Netherlands). Before microscopic observation, the samples were prepared based on the previously described procedure.[82] Briefly, the hydrogels were fixed in 3% glutaraldehyde (Agar Scientific, Wetzlar) for at least 1 h at room temperature and washed in 0.1 M Sorensen's Phosphate Buffer (Merck, Darmstadt) for 15 min. Then, the samples were dehydrated using ascending ethanol dilutions (10 min – 30%; 10 min – 50%; 10 min – 70%; 10 min – 90% and 3 × 10 min – 100% ethanol). Finally, critical point drying was performed in liquid CO_2, while coating with a 10 nm gold/palladium layer was achieved using a Sputter Coater (Sputter Coater EM SCD500, Leica, Wetzlar).

Statistical Analysis: The results were presented as mean ± standard deviation. Comparisons between the various sets of data were carried out using OriginPro 2018 (Originlab Corporation, Northampton, USA). ANOVA tests were performed in order to study significant differences within groups and comparison between groups with Tukey's post-hoc test. Significance level of $p < 0.05$ (*) was given.

Supporting Information

Supporting Information is available from the Wiley Online Library or from the author.

Acknowledgements

H.F and M.W. acknowledged the financial support of the European Regional Development Fund (Interreg Euregio Maas-Rhein) of the European Union (grant EMR116). Parts of the analytical investigations were performed at the Center for Chemical Polymer Technology CPT, which was supported by the European Commission and the federal state of North Rhine Westphalia (No. 300088302). The authors would like to thank Stephan Rütten from the Electron Microscopy Facility of the Institute of Pathology, RWTH University Hospital, Aachen, Germany for his support in sample preparation and SEM analysis, Hendrik Woters and Roswitha Davtalab from the Department of Dental Materials and Biomaterials Research, RWTH Aachen University Hospital, Aachen, Germany, for their technical assistance.

Open access funding enabled and organized by Projekt DEAL.

Conflict of Interest

The authors declare no conflict of interest.

Data Availability Statement

The data that support the findings of this study are available from the corresponding author upon reasonable request.

Keywords

3D printing, aqueous-two phase systems, bicontinuous, gelatin methacryloyl, interconnected porous hydrogels

Received: December 23, 2022
Revised: June 23, 2023
Published online: July 4, 2023

[1] V. Magno, A. Meinhardt, C. Werner, *Adv. Funct. Mater.* **2020**, *30*, 2000097.
[2] N. Annabi, A. Tamayol, J. A. Uquillas, M. Akbari, L. E. Bertassoni, C. Cha, G. Camci-Unal, M. R. Dokmeci, N. A. Peppas, A. Khademhosseini, *Adv. Mater.* **2014**, *26*, 85.
[3] R. S. Stowers, S. C. Allen, L. J. Suggs, K. S. Anseth, *Proc. Natl. Acad. Sci. USA* **2015**, *112*, 1953.
[4] A. Cheng, Z. Schwartz, A. Kahn, X. Li, Z. Shao, M. Sun, Y. Ao, B. D. Boyan, H. Chen, *Tissue Eng. – Part B Rev.* **2019**, *25*, 14.
[5] K. J. De France, F. Xu, T. Hoare, *Adv. Healthcare Mater.* **2018**, *7*, 1700927.
[6] E. Nicol, *Biomacromolecules* **2021**, *22*, 1325.
[7] Q. L. Loh, C. Choong, *Tissue Eng. – Part B Rev.* **2013**, *19*, 485.
[8] O. Oliviero, M. Ventre, P. A. Netti, *Acta Biomater.* **2012**, *8*, 3294.
[9] B. B. Mandal, S. C. Kundu, *Biomaterials* **2009**, *30*, 2956.
[10] C. M. Murphy, M. G. Haugh, F. J. O'Brien, *Biomaterials* **2010**, *31*, 461.
[11] F. Causa, P. A. Netti, L. Ambrosio, *Biomaterials* **2007**, *28*, 5093.
[12] L. R. Madden, D. J. Mortisen, E. M. Sussman, S. K. Dupras, J. A. Fugate, J. L. Cuy, K. D. Hauch, M. A. Laflamme, C. E. Murry, B. D. Ratner, *Proc. Natl. Acad. Sci* **2010**, *107*, 15211.
[13] G. L. Ying, N. Jiang, S. Maharjan, Y. X. Yin, R. R. Chai, X. Cao, J. Z. Yang, A. K. Miri, S. Hassan, Y. S. Zhang, *Adv. Mater.* **2018**, *30*, 1805460.
[14] R. Y. Kannan, H. J. Salacinski, K. Sales, P. Butler, A. M. Seifalian, *Biomaterials* **2005**, *26*, 1857.
[15] P. Carmeliet, R. K. Jain, *Nature* **2000**, *407*, 249.
[16] N. Annabi, J. W. Nichol, X. Zhong, C. Ji, S. Koshy, A. Khademhosseini, F. Dehghani, *Tissue Eng. – Part B Rev.* **2010**, *16*, 371.
[17] S. V. Murphy, A. Atala, *Nat. Biotechnol.* **2014**, *32*, 773.
[18] M. Zhou, M. Li, J. Jiang, N. Gao, F. Tian, W. Zhai, *Adv. Eng. Mater.* **2021**, *24*, 2101027.
[19] Z. Ataie, S. Kheirabadi, J. W. Zhang, A. Kedzierski, C. Petrosky, R. Jiang, C. Vollberg, A. Sheikhi, *Small* **2022**, *18*, 2202390.
[20] X. Li, B. Liu, B. Pei, J. Chen, D. Zhou, J. Peng, X. Zhang, W. Jia, T. Xu, *Chem. Rev.* **2020**, *120*, 10793.
[21] S. S. Ribeiro, N. Samanta, S. Ebbinghaus, J. C. Marcos, *Nat. Rev. Chem.* **2019**, *3*, 552.
[22] Y. Chao, H. C. Shum, *Chem. Soc. Rev.* **2020**, *49*, 114.
[23] Y. Chao, S. Y. Mak, S. Rahman, S. Zhu, H. C. Shum, *Small* **2018**, *14*, 1802107.
[24] D. L. Elbert, *Acta Biomater.* **2011**, *7*, 31.
[25] N. Broguiere, A. Husch, G. Palazzolo, F. Bradke, S. Madduri, M. Zenobi-Wong, *Biomaterials* **2019**, *200*, 56.
[26] R. L. Thankamony, X. Li, X. Fan, G. Sheng, X. Wang, S. Sun, X. Zhang, Z. Lai, *ACS Appl. Mater. Interfaces* **2018**, *10*, 44041.
[27] M. Li, X. Li, V. Tung, Y. Li, Z. Lai, *ACS Appl. Energy Mater.* **2020**, *3*, 2510.
[28] R. Mastrangelo, D. Chelazzi, G. Poggi, E. Fratini, L. P. Buemi, M. L. Petruzzellis, P. Baglioni, *Proc. Natl. Acad. Sci. USA* **2020**, *117*, 7011.
[29] H. Tavana, A. Jovic, B. Mosadegh, Q. Y. Lee, X. Liu, K. E. Luker, G. D. Luker, S. J. Weiss, S. Takayama, *Nat. Mater.* **2009**, *8*, 736.
[30] G. Bao, T. Jiang, H. Ravanbakhsh, A. Reyes, Z. Ma, M. Strong, H. Wang, J. M. Kinsella, J. Li, L. Mongeau, *Mater. Horiz.* **2020**, *7*, 2336.
[31] L. Shao, Q. Gao, C. Xie, J. Fu, M. Xiang, Z. Liu, L. Xiang, Y. He, *Bio-Design Manuf* **2020**, *3*, 30.
[32] A. Mostafavi, M. Samandari, M. Karvar, M. Ghovvati, Y. Endo, I. Sinha, N. Annabi, A. Tamayol, *Appl. Phys. Rev.* **2021**, *8*, 041415.
[33] L. Ouyang, J. P. Wojciechowski, J. Tang, Y. Guo, M. M. Stevens, *Adv. Healthcare Mater.* **2022**, 2200027.
[34] G. Ying, N. Jiang, C. Parra-Cantu, G. Tang, J. Zhang, H. Wang, S. Chen, N. P. Huang, J. Xie, Y. S. Zhang, *Adv. Funct. Mater.* **2020**, *30*, 2003740.
[35] S. Yi, Q. Liu, Z. Luo, J. J. He, H. Ma, W. Li, D. Wang, C. Zhou, C. E. Garciamendez, L. Hou, J. Zhang, Y. S. Zhang, *Small* **2022**, *18*, 2106357.
[36] G. Ying, J. Manríquez, D. Wu, J. Zhang, N. Jiang, S. Maharjan, D. H. Hernández Medina, Y. S. Zhang, *Mater. Today Bio* **2020**, *8*, 100074.
[37] D. Loessner, C. Meinert, E. Kaemmerer, L. C. Martine, K. Yue, P. A. Levett, T. J. Klein, F. P. W. Melchels, A. Khademhosseini, D. W. Hutmacher, *Nat. Protoc.* **2016**, *11*, 727.
[38] B. Grigoryan, S. J. Paulsen, D. C. Corbett, D. W. Sazer, C. L. Fortin, A. J. Zaita, P. T. Greenfield, N. J. Calafat, J. P. Gounley, A. H. Ta, F. Johansson, A. Randles, J. E. Rosenkrantz, J. D. Louis-Rosenberg, P. A. Galie, K. R. Stevens, J. S. Miller, *Science* **2019**, *364*, 458.
[39] B. Kong, Y. Chen, R. Liu, X. Liu, C. Liu, Z. Shao, L. Xiong, X. Liu, W. Sun, S. Mi, *Nat. Commun.* **2020**, *11*, 1435.
[40] A. Erdem, M. A. Darabi, R. Nasiri, S. Sangabathuni, Y. N. Ertas, H. Alem, V. Hosseini, A. Shamloo, A. S. Nasr, S. Ahadian, M. R. Dokmeci, A. Khademhosseini, N. Ashammakhi, *Adv. Healthcare Mater.* **2020**, *9*, 1901794.
[41] Z. Li, S. Zhang, Y. Chen, H. Ling, L. Zhao, G. Luo, X. Wang, M. C. Hartel, H. Liu, Y. Xue, R. Haghniaz, K. J. Lee, W. Sun, H. J. Kim, J. Lee, Y. Zhao, Y. Zhao, S. Emaminejad, S. Ahadian, N. Ashammakhi, M. R. Dokmeci, Z. Jiang, A. Khademhosseini, *Adv. Funct. Mater.* **2020**, *30*, 2003601.
[42] K. Yue, G. Trujillo-de Santiago, M. M. Alvarez, A. Tamayol, N. Annabi, A. Khademhosseini, *Biomaterials* **2015**, *73*, 254.
[43] X. Yang, A. Li, D. Li, Y. Guo, L. Sun, *Trends Food Sci. Technol.* **2021**, *109*, 197.
[44] J. Weiss, H. Salminen, P. Moll, C. Schmitt, *Adv. Colloid Interface Sci.* **2019**, *271*, 101987.
[45] M. Vis, V. F. D. Peters, R. H. Tromp, B. H. Erné, *Langmuir* **2014**, *30*, 5755.
[46] M. Vis, V. F. D. Peters, E. M. Blokhuis, H. N. W. Lekkerkerker, B. H. Erné, R. H. Tromp, *Phys. Rev. Lett.* **2015**, *115*, 078303.
[47] S. R. Caliari, J. A. Burdick, *Nat. Methods* **2016**, *13*, 405.
[48] P. Swain, A. Ronghe, U. Bhutani, S. Majumdar, *J. Phys. Chem. B* **2019**, *123*, 1186.
[49] W. J. Frith, *Adv. Colloid Interface Sci.* **2010**, *161*, 48.
[50] O. Chaudhuri, S. T. Koshy, C. Branco Da Cunha, J. W. Shin, C. S. Verbeke, K. H. Allison, D. J. Mooney, *Nat. Mater.* **2014**, *13*, 970.
[51] J. H. Wen, L. G. Vincent, A. Fuhrmann, Y. S. Choi, K. C. Hribar, H. Taylor-Weiner, S. Chen, A. J. Engler, *Nat. Mater.* **2014**, *13*, 979.
[52] O. Chaudhuri, L. Gu, D. Klumpers, M. Darnell, S. A. Bencherif, J. C. Weaver, N. Huebsch, H. P. Lee, E. Lippens, G. N. Duda, D. J. Mooney, *Nat. Mater.* **2016**, *15*, 326.
[53] S. Tang, B. M. Richardson, K. S. Anseth, *Prog. Mater. Sci.* **2021**, *120*, 100738.
[54] D. F. D. Campos, A. Blaeser, A. Korsten, S. Neuss, J. Jäkel, M. Vogt, H. Fischer, D. F. Duarte Campos, A. Blaeser, A. Korsten, S. Neuss, J. Jäkel, M. Vogt, H. Fischer, *Tissue Eng. – Part A* **2015**, *21*, 740.
[55] J. Seo, J. Y. Shin, J. Leijten, O. Jeon, A. Bal Öztürk, J. Rouwkema, Y. Li, S. R. Shin, H. Hajiali, E. Alsberg, A. Khademhosseini, *ACS Appl. Mater. Interfaces* **2018**, *10*, 13293.
[56] J. Yin, M. Yan, Y. Wang, J. Fu, H. Suo, *ACS Appl. Mater. Interfaces* **2018**, *10*, 6849.
[57] H. Ko, K. Suthiwanich, H. Mary, S. Zanganeh, S. K. Hu, S. Ahadian, Y. Yang, G. Choi, K. Fetah, Y. Niu, J. J. Mao, A. Khademhosseini, *Biofabrication* **2019**, *11*, 025014.

[58] C. D. O'Connell, B. Zhang, C. Onofrillo, S. Duchi, R. Blanchard, A. Quigley, J. Bourke, S. Gambhir, R. Kapsa, C. Di Bella, P. Choong, G. G. Wallace, *Soft Matter* **2018**, *14*, 2142.
[59] C. F. Guimarães, L. Gasperini, A. P. Marques, R. L. Reis, *Nat. Rev. Mater.* **2020**, *5*, 351.
[60] I. Noshadi, S. Hong, K. E. Sullivan, E. Shirzaei Sani, R. Portillo-Lara, A. Tamayol, S. R. Shin, A. E. Gao, W. L. Stoppel, L. D. Black, A. Khademhosseini, N. Annabi, *Biomater. Sci.* **2017**, *5*, 2093.
[61] J. C. C. J. C. Stendahl, M. S. M. S. Rao, M. O. M. O. O. Guler, S. I. S. I. I. Stupp, *Adv. Funct. Mater.* **2006**, *16*, 499.
[62] M. Djabourov, K. Nishinari, S. Ross-Murphy, in *Physical Gels from Biological Synthetic Polymers* (Eds.: M. Djabourov, K. Nishinari, S. Ross–Murpohy), Cambridge University Press, New York, United States of America **2013**, pp. 287.
[63] S. Aveic, R. Davtalab, M. Vogt, M. Weber, P. Buttler, G. P. Tonini, H. Fischer, *Acta Biomater.* **2019**, *88*, 527.
[64] P. Erkoc, F. Seker, T. Bagci-Onder, S. Kizilel, *Macromol. Biosci.* **2018**, *18*, 1700369.
[65] M. Boyd-Moss, K. Firipis, C. D. O'Connell, A. Rifai, A. Quigley, G. Boer, B. M. Long, D. R. Nisbet, R. J. Williams, *Mater. Chem. Front.* **2021**, *5*, 8025.
[66] S. Nemec, J. Lam, J. Zhong, C. Heu, P. Timpson, Q. Li, J. Youkhana, G. Sharbeen, P. A. Phillips, K. A. Kilian, *Adv. Biol.* **2021**, *5*, 2000525.
[67] R. Krencik, K. Seo, J. V. van Asperen, N. Basu, C. Cvetkovic, S. Barlas, R. Chen, C. Ludwig, C. Wang, M. E. Ward, L. Gan, P. J. Horner, D. H. Rowitch, E. M. Ullian, *Stem Cell Rep.* **2017**, *9*, 1745.
[68] M. F. Butler, M. Heppenstall-Butler, *Biomacromolecules* **2001**, *2*, 812.
[69] N. Lorén, A. M. Hermansson, M. A. K. Williams, L. Lundin, T. J. Foster, C. D. Hubbard, A. H. Clark, I. T. Norton, E. T. Bergström, D. M. Goodall, *Macromolecules* **2001**, *34*, 289.
[70] L. Guo, R. H. Colby, C. P. Lusignan, A. M. Howe, *Macromolecules* **2003**, *36*, 10009.
[71] A. Hori, Y. Watabe, M. Yamada, Y. Yajima, R. Utoh, M. Seki, *ACS Appl. Bio Mater.* **2019**, *2*, 2237.
[72] M. Vis, V. F. D. Peters, B. H. Erné, R. H. Tromp, *Macromolecules* **2015**, *48*, 2819.
[73] M. Vis, V. F. D. Peters, E. M. Blokhuis, H. N. W. Lekkerkerker, B. H. Erné, R. H. Tromp, *Macromolecules* **2015**, *48*, 7335.
[74] C. Ji, A. Khademhosseini, F. Dehghani, *Biomaterials* **2011**, *32*, 9719.
[75] J. W. Nichol, S. T. Koshy, H. Bae, C. M. Hwang, S. Yamanlar, A. Khademhosseini, *Biomaterials* **2010**, *31*, 5536.
[76] A. Khan, K. A. Alamry, *Carbohydr. Res.* **2021**, *506*, 108368.
[77] B. H. Lee, H. Shirahama, N. J. Cho, L. P. Tan, *RSC Adv.* **2015**, *5*, 106094.
[78] A. Blaeser, D. F. Duarte Campos, U. Puster, W. Richtering, M. M. Stevens, H. Fischer, *Adv. Healthcare Mater.* **2016**, *5*, 326.
[79] H. Stratesteffen, M. Köpf, F. Kreimendahl, A. Blaeser, S. Jockenhoevel, H. Fischer, *Biofabrication* **2017**, *9*, 045002.
[80] I. Lauria, M. Höner, S. Kant, R. Davtalab, T. Weik, K. Sternberg, H. Fischer, *J. Biomed. Mater. Res. – Part A* **2018**, *106*, 180.
[81] J. Stuckner, K. Frei, I. McCue, M. J. Demkowicz, M. Murayama, *Comput. Mater. Sci.* **2017**, *139*, 320.
[82] S. Aveic, S. Janßen, R. Nasehi, M. Seidelmann, M. Vogt, M. Pantile, S. Rütten, H. Fischer, *Biomater. Sci.* **2021**, *9*, 1716.